

POLITECNICO DI TORINO

Master's Degree in Aerospace Engineering



Master's Degree Thesis

Design and Computational Study of Supersonic Turbines for Rocket Engines

Supervisors

Prof. Andrea FERRERO

Dr. Alessandro CAPPIELLO

Dr. Matteo PINI

Candidate

Sofia LOMBARDI

Academic Year 2024 - 2025

Abstract

The optimization of supersonic turbines is a rapidly evolving field of research whose main objectives are improving the performance of the turbine and increasing the life of the machine. Achieving these goals becomes even more challenging when high-energy working fluids are used, as in the rocket industry.

This project focuses on the aerodynamic design and numerical analysis of supersonic turbines, encompassing turbine mean-line design, design of vane and blade profiles, culminating in computational fluid dynamics simulations of the blade passages. The project aims at investigating the impact of design parameters on the flow structure of supersonic turbines, as well as on the reliability of isolated stator calculations -very widespread for stator shape optimization- compared to coupled stator-rotor calculations. Therefore, particular attention is given to the fluid-dynamic phenomena occurring at the stator outlet and their interaction with the rotor leading edge.

To accomplish these objectives, three turbine stages with different expansion ratios are designed from scratch. The design process is based on non-dimensional parameters, including the flow coefficient, loading coefficient and degree of reaction, leveraging an in-house mean line design code. Design maps are then generated for the three cases to identify the optimal design points.

Subsequently, inverse design methods implemented in in-house codes based on the method of characteristics are used to compute the shape of vane and blade passages.

Finally, CFD simulations are performed using the SU2 software. The analysis begins with isolated stator calculations, followed by coupled stator-rotor calculations, employing different numerical approaches to examine the flow field within the blade passages. Attention is paid to the mesh resolution to enable the analysis of the shock structure and development of the boundary layer. The findings of this study contribute to a deeper understanding of supersonic turbine fluid dynamics and offer potential improvements in the design of high-performance turbomachinery, particularly for aerospace and energy applications.

Acknowledgements

I would like to express my sincere gratitude to Dr. Alessandro Cappiello for his expert guidance and constant support throughout this thesis project. His contribution has been essential not only for the development of the work itself but also for introducing me to the world of research, which I now approach with great interest and motivation.

I also want to thank Dr. Matteo Pini for choosing me for this project and giving me the chance to carry out my thesis abroad at Delft University of Technology.

Finally, I would like to thank Prof. Andrea Ferrero for introducing me with passion and expertise to the field of fluid dynamics, helping me discover a deep interest in this discipline.

Table of Contents

List of Tables	VIII
List of Figures	IX
Acronyms	XIV
1 Introduction	2
1.1 Study Objective	4
1.2 Research Plan	5
2 Mean Line Design	8
2.1 Boundary Conditions Definition	9
2.2 TurboSim	13
2.2.1 Methodology	14
2.2.2 Stage Layout and Numerical Framework	14
2.2.3 Loss Models	16
2.2.4 Mean Line Analysis	18
2.2.5 Chosen Designs	22
3 Blade Design	29
3.1 Method of Characteristics	29
3.2 Supersonic Stator	32
3.2.1 Nozzle Design	33
3.2.2 Axial Stator Design	37
3.3 Supersonic rotor	38
4 Computational Fluid Dynamics of Supersonic Turbines	42
4.1 Flow Field in Supersonic Turbines	42
4.2 Navier-Stokes Equations	44
4.3 Turbulence Modelling	45
4.3.1 Two-equation transport models	48

4.3.2	One-equation transport model	50
4.3.3	CFL Condition	51
4.4	Convective Fluxes	52
4.4.1	Roe method	53
4.4.2	JST method	53
4.5	Boundary layer resolution requirements	54
4.6	Stator-Rotor Interaction Methods	55
4.6.1	Mixing Plane	56
4.6.2	Harmonic Balance	57
5	Computational Fluid Dynamics Simulations	61
5.1	Mesh Generation	61
5.2	Mesh Sensitivity	62
5.3	Isolated Stators Analysis	63
5.3.1	First Stator Results	65
5.3.2	Second Stator Results	68
5.3.3	Third Stator Results	69
5.4	Stator-Rotor Analysis	70
5.4.1	Mixing Plane Method Results	70
5.4.2	Harmonic Balance Method Results	73
5.4.3	Results Comparison	76
6	Conclusions	80
6.1	Summary	80
6.2	Future Developments	81
A	Design Maps	83
	Bibliography	92

List of Tables

2.1	Design Characteristics	24
3.1	Comparison of TurboSim and OpenMOC stator outlet Mach numbers for different expansion ratios.	37
5.1	Main simulation parameters of the axial stators	64
5.2	Second turbine HB parameters	73

List of Figures

1.1	Supersonic Turbines [1]	2
1.2	Open Cycle [6]	4
1.3	Span-wise Mach and flow angle distribution at the stator outlet [4] .	4
1.4	Isolated stator analysis example [4]	5
2.1	Turbine stage velocity diagrams [7].	10
2.2	h-s diagram for a turbine stage [7].	10
2.3	Rotor inlet relative Mach number distribution	12
2.4	Exemplary turbine stage geometry: blade-to-blade and meridional views [8].	15
2.5	Simplified velocity distribution in the blade-to-blade plane [8]. . . .	16
2.6	Variation of turbine static density ratio and hub-tip diameter ratio with pressure ratio [10].	20
2.7	Peripheral speed at midspan	23
2.8	Stator Outlet flow angle	23
2.9	Mach numbers at rotor inlet	24
2.10	Stator Outlet Mach numbers	24
2.11	Mean diameters	25
2.12	Heights at Stator Outlet	25
2.13	α at stator outlet	25
2.14	α at rotor outlet	25
2.15	Total-to-static efficiency	25
2.16	Loading Coefficient ψ	25
2.17	Peripheral velocities at midspan	26
2.18	Peripheral velocities at tip	26
2.19	Low β stage, velocity triangle	26
2.20	Medium β stage, velocity triangle	26
2.21	High β stage, velocity triangle	26
3.1	Supersonic nozzle [2]	32

3.2	Method of characteristics implemented to design the divergent section of the supersonic nozzle [14]	35
3.3	Peripheral speed at midspan [17]	36
3.4	Stator Outlet flow angle [17]	36
3.5	Divergent section of the low expansion ratio vane	37
3.6	Divergent section of the medium expansion ratio vane	37
3.7	Divergent section of the high expansion ratio vane	37
3.8	Stator Blade of the low pressure ratio turbine	38
3.9	Stator Blade of the medium pressure ratio turbine	38
3.10	Stator Blade of the high pressure ratio turbine	38
3.11	Supersonic axial rotor blade sections [19]	39
3.12	Rotor blade of the medium pressure ratio turbine	40
3.13	Rotor blade of the high pressure ratio turbine	40
4.1	Static pressure contours and schematic of shock waves [20]	43
4.2	SU2 analysis example with Mixing Plane [28]	56
5.1	First stator coarse mesh	62
5.2	Entropy Generation	63
5.3	Entropy Generation Variation	63
5.4	Mach number distribution of the first stator	65
5.5	Pressure distribution of the first stator	65
5.6	Sonic Line	66
5.7	Shock-Boundary layer interaction	66
5.8	BL separation	67
5.9	BL reattachment	67
5.10	Wake and Boundary Layer	67
5.11	Residuals of isolated first stator	67
5.12	Mach number distribution of the second stator	68
5.13	Pressure distribution of the second stator	68
5.14	Residuals of isolated second stator	68
5.15	Mach number distribution of the third stator	69
5.16	Pressure distribution of the third stator	69
5.17	Residuals of isolated third stator	69
5.18	Absolute Mach number distribution of the second stage	70
5.19	Pressure distribution of the second stage	70
5.20	Relative Mach Distribution of the second stage	71
5.21	Zoomed-in view	71
5.22	Relative Mach number distribution of the third stage	72
5.23	Pressure Distribution of the third stage	72
5.24	Residuals steady stator-rotor analysis.	72

5.25	Relative Mach number distribution of the first time instance	73
5.26	Density gradient of the first time instance	73
5.27	Relative Mach number distribution of the second time instance	74
5.28	Density gradient of the second time instance	74
5.29	Relative Mach number distribution of the third time instance	74
5.30	Density gradient of the third time instance	74
5.31	Stator blade pressure distribution at time instant t_0	75
5.32	Stator blade pressure distribution at time instant t_1	75
5.33	Stator blade pressure distribution at time instant t_2	75
5.34	Rotor blade pressure distribution at time instant t_0	75
5.35	Rotor blade pressure distribution at time instant t_1	75
5.36	Rotor blade pressure distribution at time instant t_2	75
5.37	Mach number distribution of the second stator with higher down- stream pressure	76
5.38	Tangential pressure distributions	77
5.39	Tangential pressure distributions of the unsteady simulations	77
A.1	Rotor inlet Mach number	83
A.2	Rotor outlet Mach number	83
A.3	Stator outlet Mach number	84
A.4	Peripheral speed	84
A.5	Boundary Layer Losses	84
A.6	Total-to-static Efficiency	84
A.7	Stator outlet and rotor inlet axial Mach number	84
A.8	Rotor outlet axial Mach number	84
A.9	Rotor outlet absolute Mach number	85
A.10	Rotor outlet flow angle [$^{\circ}$]	85
A.11	Stator outlet flow angle [$^{\circ}$]	85
A.12	Stator Inlet Blade Height (H_0) [m]	86
A.13	Stator Outlet Blade Height ($H_1 = H_2$) [m]	86
A.14	Rotor Outlet Blade Height (H_3) [m]	86
A.15	Mean Diameter [m]	86
A.16	Rotor inlet Mach number	87
A.17	Rotor outlet Mach number	87
A.18	Stator outlet Mach number	87
A.19	Peripheral speed	87
A.20	Total-to-static Efficiency	87
A.21	Rotor outlet absolute Mach number	88
A.22	Rotor outlet flow angle [$^{\circ}$]	88
A.23	Stator outlet flow angle [$^{\circ}$]	88
A.24	Rotor inlet Mach number	89

A.25 Rotor outlet Mach number	89
A.26 Stator outlet Mach number	89
A.27 Peripheral speed	89
A.28 Total-to-static efficiency	89
A.29 Rotor outlet absolute Mach number	90
A.30 Rotor outlet flow angle [°]	90
A.31 Stator outlet flow angle [°]	90

Acronyms

CFD

Computational Fluid Dynamics

MOC

Method of Characteristics

ORC

Organic Ranking Cycle

PDE

Partial Differential Equations

NS

Navier-Stokes

DNS

Direct Numerical Simulations

LES

Large Eddy Simulations

CFL

Courant-Friedrichs-Lewy

RANS

Reynolds-Averaged Navier-Stokes

JST

Jameson-Schmidt-Turkel

SA

Spalart-Allmaras

MUSCL

Monotone Upstream-Centred Schemes for Conservation Laws

BPF

Blade Passing Frequency

URANS

Unsteady Reynolds-Averaged Navier-Stokes

BL

Boundary Layer

MP

Mixing Plane

HB

Harmonic Balance

Chapter 1

Introduction

Supersonic turbines are the subject of increasing research because of their suitability for applications involving high-energy fluids, low molecular weight and significant expansion rates, as well as the ability to deliver large specific work through high expansion ratios.

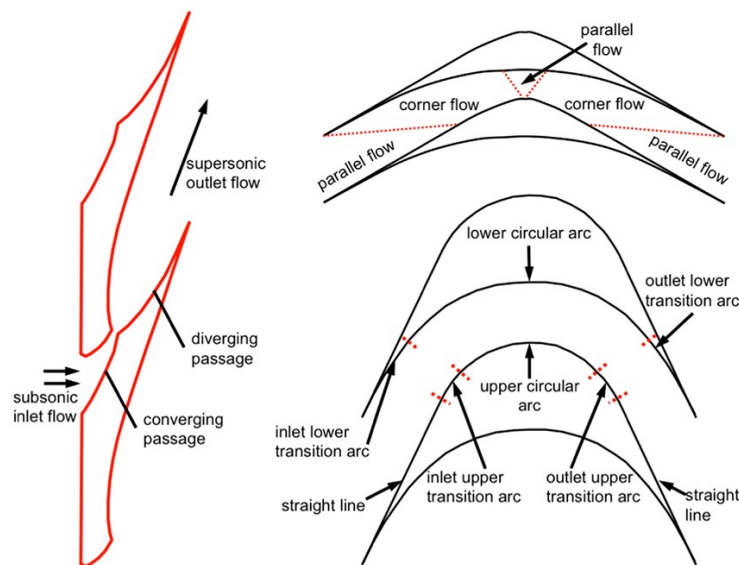


Figure 1.1: Supersonic Turbines [1]

A feature of these turbines is the presence of supersonic relative velocities at the rotor inlet, combined with a small amount of driving fluid and a limited number of stages, typically not exceeding three. High jet velocities and short blade lengths generate radial pressure gradients that drive low-energy fluid towards the hub,

resulting in additional losses that contribute to a lower static efficiency.

They are affected by high thermal loads and mechanical stresses for operating in extreme conditions: they require advanced materials and cooling techniques to ensure structural integrity and a longer operational life [2][3].

The main applications of these turbines concern the following systems:

1. Rocket turbopump systems
2. Open-cycle auxiliary power systems for space
3. High-temperature organic Rankine cycle power systems

Supersonic turbines are commonly used in rocket turbopumps due to their high expansion ratios and their compactness and lightness. Because of that, they are typically of axial configuration, with a single or double stage and the flow in either the stator and rotor passages is highly supersonic [4].

The turbopump systems play a key role in driving propellants to the combustion chamber at the required pressure and flow rate. The turbine must provide sufficient power to pressurise the fuel and oxidizer, with minimal turbine mass flow. The latter is important to align with the principles of open-cycle configurations, as it decreases engine thrust [5].

In an open cycle, also known as a gas generator cycle, a portion of the propellant is combusted separately in a pre-burner to drive the turbine, after which it is expelled rather than being fully directed to the combustion chamber. This design simplifies the overall system and improves reliability, although it reduces efficiency because part of the energy is lost with the exhaust gases. Nevertheless, the open-cycle configuration offers several advantages, including a simpler layout, lower operational temperatures and easier maintenance.

The efficiency of the supersonic turbine is usually much lower than that of the conventional turbine [3]. However, research is growing to try to optimise performance and make it increasingly suitable for this type of system. The preliminary design is indeed crucial in order to improve efficiency and reduce losses.

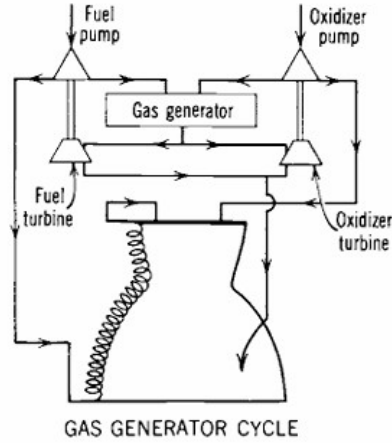


Figure 1.2: Open Cycle [6]

1.1 Study Objective

The operation of supersonic turbines deals with difficult aspects due to the complex flow conditions within the blade passages, caused by the supersonic Mach number at the vane outlet. In fact, the stator outlet flow introduces significant non-uniformity due to the interactions between expansion fans and shock waves generated at the stator trailing edge, along with the reflected shocks originating from the suction side of the adjacent vanes.

Minimizing the flow non-uniformities and the shock intensities at the stator outlet is therefore a critical consideration. For example, in figure 1.3, the pitch-wise distribution of the outlet Mach number and flow angle are compared for a baseline and an optimised stator blade, as explained in [4].

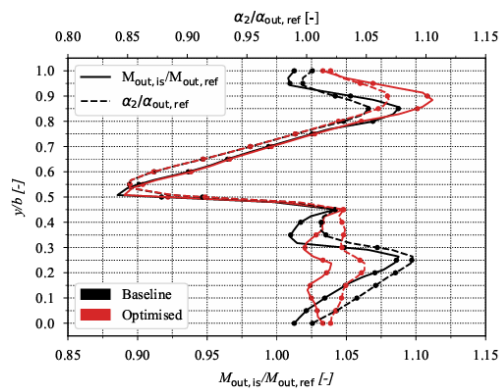


Figure 1.3: Span-wise Mach and flow angle distribution at the stator outlet [4]

To study these effects, an isolated stator is often optimised, as this approach is computationally more efficient.

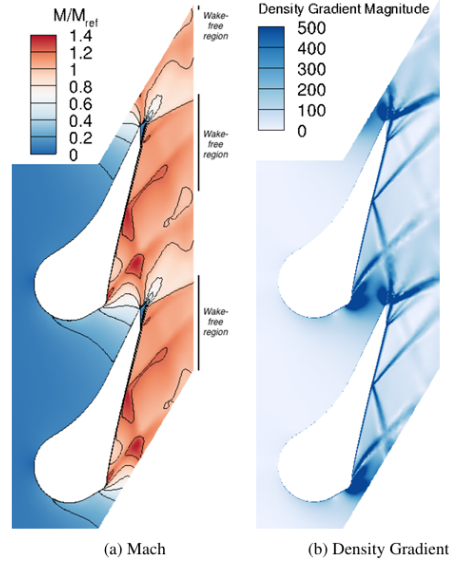


Figure 1.4: Isolated stator analysis example [4]

However, these questions could arise:

1. Is the pitch-wise distribution of an isolated stator representative of the coupled stator-rotor flow field?
2. How close are the results to the ones obtained with stator-rotor calculations?
3. Are there any parameters that can determine the reliability of the method?

The purpose of this work is to address these questions, starting from the mean line design of the turbine and progressing to CFD analyses of the isolated stator and the coupled stator-rotor system, both in steady and unsteady conditions.

1.2 Research Plan

Several parameters have been identified as potential subjects of investigation, with the objective of examining their influence on the stator-rotor interaction and their role in determining the reliability of CFD analyses of the isolated stator:

1. Rotor inlet relative Mach number
2. Stator-Rotor axial gap

3. Rotor LE-to-pitch ratio
4. Stator TE-to-pitch ratio
5. Blade metal angle at rotor inlet

The first parameter is chosen as the fundamental subject of study and on the basis of this all subsequent design is carried out, keeping the other parameters constant.

To investigate the rotor inlet relative Mach number, the aim is to design three turbine stages for different values of this quantity:

1. $M_{rel,rotor\ inlet}=0.9$
2. $M_{rel,rotor\ inlet}=1.15$
3. $M_{rel,rotor\ inlet}=1.3$

Once these three stages are designed, the next step involves the comparison of the stator outlet flow field. It begins with steady-state analysis of the isolated stator and then it moves to fully unsteady simulations, including harmonic balance.

Chapter 2

Mean Line Design

The mean line analysis is a preliminary design method to determine the main thermodynamic characteristics of the turbine along the mean line flow path within the machine. It represents the first fundamental step of the aerodynamic design process of a turbomachine, following the conceptual phase. This approach considers the flow as a one-dimensional problem, providing a simplified but effective representation to estimate the initial performance of the turbine.

Three key non-dimensional parameters are linked to the shape of the turbine velocity triangles and are used to fix the preliminary design of a turbine stage [7]:

1. Design Flow Coefficient
2. Stage Loading Coefficient
3. Stage Reaction

The flow coefficient is defined as the ratio of the meridional flow velocity to the blade speed, $\phi = C_m/U$, but in a purely axial-flow machine it is $\phi = C_x/U$ [7].

The loading coefficient is expressed as the proportion of the change in stagnation enthalpy across a stage to the square of the blade velocity, $\psi = \Delta h/U^2$. In an adiabatic turbine, the change in stagnation enthalpy corresponds to the specific work output, ΔW [7]. The Euler work equation can be applied and can be written in a general form as in the equation 2.1, or for a purely axial machine it is as in the equation 2.2.

$$\Delta W_x = (h_{01} - h_{02}) = U_1 c_{\theta 1} - U_2 c_{\theta 2} \quad (2.1)$$

$$\Delta h_0 = \Delta(U c_\theta) = U \Delta c_\theta \quad (2.2)$$

Consequently, the loading coefficient can be written as in the equation 2.34.

$$\psi = \frac{\Delta c_\theta}{U} \quad (2.3)$$

where Δc_θ is the change in the absolute tangential velocity through the rotor. In rocket turbopumps applications, a high stage loading coefficient is required because it allows the turbine to generate the required work output with fewer stages, thereby meeting the compactness requirement.

The degree of reaction is defined as the ratio between the static enthalpy drop that occurs in the rotor and the static enthalpy drop throughout the stage as in the equation 2.4.

$$R = \frac{h_2 - h_3}{h_1 - h_3} \quad (2.4)$$

Considering nearly isentropic transformations and ignoring compressibility effects, the reaction can be approximated as in 2.5.

$$R \approx \frac{p_2 - p_3}{p_1 - p_3} \quad (2.5)$$

2.1 Boundary Conditions Definition

To carry out the mean line design, an in-house code developed by TU Delft, known as TurboSim, is used. This software requires input boundary conditions to be specified within its configuration file. Therefore, it is essential to define these conditions appropriately based on the specific context and application.

In particular, the required conditions are:

- Working fluid
- Reduced temperature (T_r)
- Reduced pressure (P_r)
- Expansion ratio or volumetric flow ratio
- R_{hub}/R_{tip}

In order to define the previous quantities for each of the three turbine stages and to reach the target Mach numbers, some typical values for supersonic turbines have been fixed as follows, referring to figures 2.2 and 2.1:

- $P_{01} = 80bar$

- $T_{01} = 1000K$
- $R = 0.25$
- $\alpha_2 = 72^\circ$

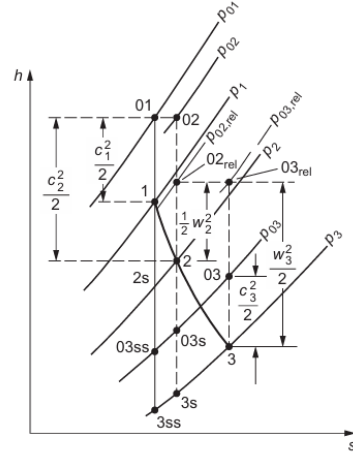
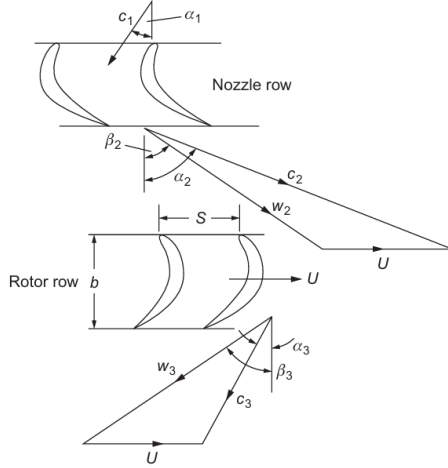


Figure 2.1: Turbine stage velocity diagrams [7].

Figure 2.2: h-s diagram for a turbine stage [7].

Isentropic relations are applied by varying the peripheral velocity U and the static pressure downstream of the rotor P_3 in the following ranges:

- $P_3 = [10^5, 3 * 10^6] Pa$
- $U = [200, 600] m/s$

$$\frac{T_3}{T_{01}} = \left(\frac{P_3}{P_{01}} \right)^{\frac{\gamma-1}{\gamma}} \quad (2.6)$$

$$h_3 = c_p T_3 \quad (2.7)$$

$$h_{01} = c_p T_{01} \quad (2.8)$$

$$R = \frac{h_2 - h_3}{h_{01} - h_3} \quad (2.9)$$

$$h_2 = h_3 + R(h_{01} - h_3) \quad (2.10)$$

And, as a consequence, it results:

$$c_2 = 2\sqrt{h_{01} - h_2} \quad (2.11)$$

$$c_{2x} = c_2 \cos \alpha_2 \quad (2.12)$$

$$c_{2y} = c_2 \sin \alpha_2 \quad (2.13)$$

$$w_{2x} = c_{2x} - U \quad (2.14)$$

$$w_{2y} = c_{2y} \quad (2.15)$$

$$w_2 = \sqrt{w_{2x}^2 + w_{2y}^2} \quad (2.16)$$

$$T_2 = \frac{h_2}{c_p} \quad (2.17)$$

$$a = \sqrt{\gamma RT_2} \quad (2.18)$$

$$M_{rel,rotor\ inlet} = \frac{w_2}{a_2} \quad (2.19)$$

For each combination of U and P_3 , a Mach number value is fixed.

The results of this process are illustrated in the figure 2.3, which shows the variation of the Mach number with U and P_3 .

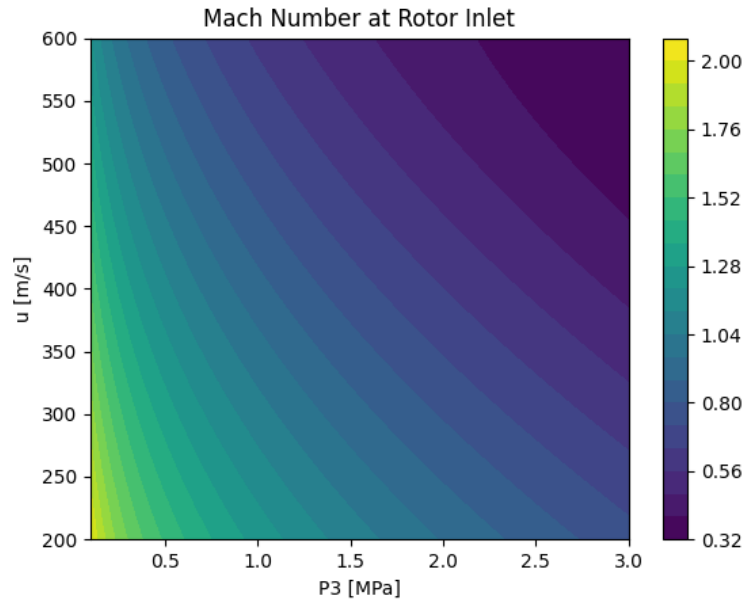


Figure 2.3: Rotor inlet relative Mach number distribution

The purpose is to choose a thermodynamic condition for each target Mach number.

The peripheral velocity is fixed in the range, performing an iterative process after the TurboSim results, to match a proper value and it results in $U = 400\text{m/s}$.

Consequently, the P_3 values for each Mach number are determined and the expansion ratios are equal to:

- $M_{rel,rotor\ inlet}=0.9 \rightarrow \beta = 5$
- $M_{rel,rotor\ inlet}=1.15 \rightarrow \beta = 16$
- $M_{rel,rotor\ inlet}=1.3 \rightarrow \beta = 30$

From this point on, the three turbines are classified as follows.

1. Low Pressure Ratio Turbine Stage
2. Medium Pressure Ratio Turbine Stage
3. High Pressure Ratio Turbine Stage

2.2 TurboSim

TurboSim is a software tool, developed by Propulsion & Power group at TU Delft, that calculates the fluid dynamic performance of turbine stages. It uses a set of dimensionless design variables, such as the flow coefficient, head coefficient, degree of reaction, expansion ratio, and other fluid-dependent parameters. The software employs a loss model based on first principles, extended to handle arbitrary flow regimes and fluids.

It is designed to address the challenges of fluid dynamic design of axial turbines operating with nonideal compressible flows. The main objective is to close the existing gap in design guidelines for unconventional turbomachinery, which cannot be adequately designed using established criteria for steam and gas turbines.

The impact of non-ideal compressible flows on axial turbine design was analysed by revising and extending the classical similarity equation to include the effects of non-ideal flow. The analysis using a dimensional stage model incorporating a fundamentals-based leakage model revealed that the molecular complexity of the fluid and the volumetric flow ratio of the stage significantly influence turbine efficiency and optimal stage configuration. In particular, compressibility effects can lead to variations in stage efficiency of up to 3-4% compared to turbines designed to operate with dilute gases. These effects can be predicted at the preliminary design stage by evaluating the pressure-volume isentropic exponent [8].

Design guidelines for conventional turbomachinery are based on efficiency maps as a function of work and flow coefficients, providing preliminary estimates of size, shape of speed triangles and fluid dynamic performance. However, for unconventional turbomachinery, such as Organic Rankine Cycle (ORC) turbines, turbines for the oil and gas industry operating with heavy molecules, supercritical CO₂ (sCO₂) compressors and high-speed compressors for refrigeration and air conditioning, such maps have not yet been established [8].

These machines deal with large gradients in thermophysical properties and non-ideal flow phenomena along the expansion process, which alters the distribution of losses. This is due to viscous friction, shocks and mixing phenomena compared to conventional turbines. Existing design practices are not sufficiently validated for non-ideal flow applications due to the large differences in flow conditions within the blade passages.

To address this shortcoming, the theoretical and numerical framework underpinning TurboSim incorporates a reduced-order stage model based on classical similarity parameters, such as work coefficient and dimensionless quantities specific to unconventional turbomachinery as the volumetric flow ratio and the pressure-volume isentropic exponent. The loss model employed is based on fundamental

principles and has been extended to cover arbitrary thermophysical fluid dynamics models [8].

As a result, TurboSim generates non-dimensional maps representing various quantities of interest, such as turbine stage efficiency.

2.2.1 Methodology

The Mach numbers of the cascades are evaluated once the velocity triangles and stage speeds have been calculated, in the typical gas turbine stage design process. The design is then iteratively adjusted to obtain stage configurations that meet mechanical and operational constraints. The same procedure can be adopted to design unconventional turbine stages, but at the expense of neglecting characteristic Mach numbers [8]. This means that while following a similar design method, the peculiarities of non-ideal fluids, such as compressibility and molecular complexity, may not be adequately considered, leading to suboptimal results. In other words, conventional design may not take into account variations in fluid behaviour, which affect flow dynamics and, consequently, turbine efficiency and performance.

For example, a turbine stage operating with a complex fluid molecule is characterised by low specific work values, but could exhibit significantly higher volumetric flow ratios than gas turbine stages. This is mainly due to the low heat capacity ratio and the high molecular weight of complex fluid. As explained in [8], the normalised work decreases as the molecular complexity of the fluid increases and it is slightly influenced by a $\alpha = \rho_{t,0}/\rho_3$ variation for highly complex fluid molecules.

This effect is also due to the thermodynamic regime of the fluid and is therefore present in the case of the supersonic turbine due to the high expansion ratios and all the phenomena involved.

Based on these considerations, it can be stated that the optimal choice of conceptual stage design parameters may depend on the fluid molecule considered and the associated thermodynamic conditions.

Therefore, the authors of the software decided to modify the classical similarity equation, making it also depend on the volumetric flow ratio (and thus expansion ratio) and isentropic pressure-volume exponent, in addition to the duty coefficient, Mach number, Reynolds number and a geometric characteristic [8].

2.2.2 Stage Layout and Numerical Framework

The three-dimensional blade geometry is assumed to consist of a series of two-dimensional airfoils, as shown in the figure 2.4, characterised by negligible thickness and a parabolic line of curvature, stacked radially according to a free vortex design.

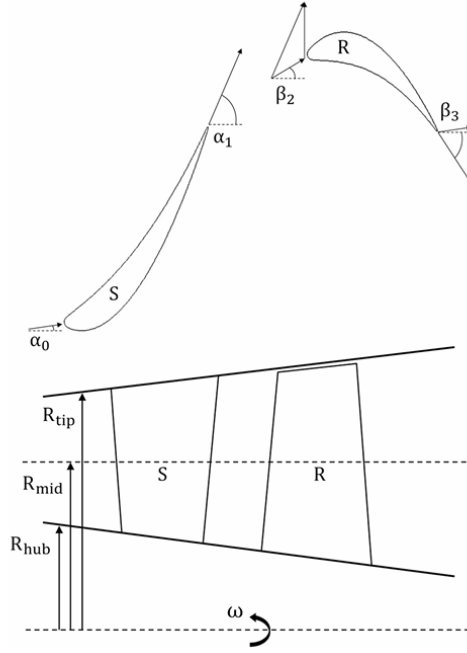


Figure 2.4: Exemplary turbine stage geometry: blade-to-blade and meridional views [8].

Blade pitch and inclination are expressed in terms of the solidity $\sigma = c/s$ and axial solidity $\sigma_{ax} = c_{ax}/s$, while the annular geometry is characterised by the blade aspect ratio $AR = (H_{in} + H_{out})/2c_{ax}$ and the hub-to-tip radius ratio. The gap between the rotor tip and the turbine case is expressed as a percentage of the blade height $2g/(H_{in} + H_{out})$, while the stator has no gap. All turbine stages are designed with constant mean radius and constant meridional speed.

The velocity triangles are uniquely determined by the choice of the total-to-static loading coefficients K_{is} , the flow coefficient ϕ , the total-to-static degree of reaction χ^* , the midspan radius variation in the rotor and the stator inlet flow angle [8]. The latter is set at $\alpha = 0$ because each turbine has one stage.

The numerical model is based on a simplified approach representing the flow distribution along the blade profile, assuming a simplified velocity profile and flow evolution along the free aperture according to a free-vortex design.

- **Velocity model:** the flow along the blade profile is represented using a simplified velocity profile, while the velocity profile parameters on pressure and suction surfaces are calculated using the circulation theorem and the tangential momentum balance.

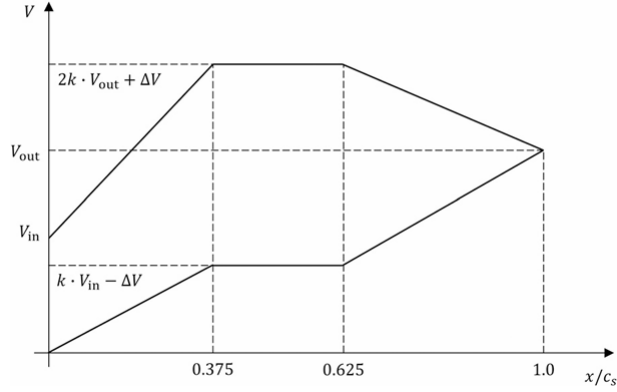


Figure 2.5: Simplified velocity distribution in the blade-to-blade plane [8].

- **Iterative Method:** the tangential moment balance is solved iteratively to account for compressibility effects and non-linearities introduced by the use of arbitrary thermodynamic models.
- **Designs generation:** a set of 400 stage configurations is generated by varying the total-to-static loading and flow coefficients to construct efficiency maps. The model is applied by specifying the expansion ratio, reduced inlet conditions and an initial estimate of the channel size relative to the average radius.
- **Simplifying assumptions:** the effect of Reynolds number is neglected since the turbine stages are assumed to operate in a fully turbulent regime. The geometric characteristics of the stage are calculated according to best practices, such as Zweifel's criterion for optimal robustness.

2.2.3 Loss Models

The proposed loss models offer a compromise between accuracy and computational complexity, making it useful for the preliminary design of axial turbines operating with non-ideal fluids. The adoption of dimensionless parameters and a formulation based on physical principles allows reliable prediction of performance, supporting the definition of optimal design guidelines [8].

- **Boundary Layer Loss.** These losses result from viscous dissipation in a two-dimensional boundary. The entropy production can be estimated as

$$\dot{S} = \int C_d \frac{\rho_e V_e^3}{T_e} dx \quad (2.20)$$

where C_d is the dissipation coefficient, which is calculated based on local flow conditions.

- **Mixing Loss.** These losses are generated by the mixing of flows with different velocities at the blade outlet. They are calculated by analysing the control volume between the throat and the downstream section, assuming uniform flow at the outlet. The law of conservation of energy and momentum is applied to estimate the entropy increase due to mixing:

$$\dot{m} = \rho_a V_a (a - \delta^*) = \rho_{\text{mix}} V_{\text{mix}} \cos \alpha_{\text{mix}} s \quad (2.21)$$

$$\dot{m} V_a - \rho_a V_a^2 \theta + P_a a + P_b t \cos \alpha_a = \dot{m} V_{\text{mix}} \cos \delta + P_{\text{mix}} s \cos \alpha_a \quad (2.22)$$

$$h_a + \frac{V_a^2}{2} = h_{\text{mix}} + \frac{V_{\text{mix}}^2}{2} \quad (2.23)$$

The boundary layer parameters are set to reference values measured in transonic cascades, i.e. $\theta/t = 0.075$ and $\delta/\theta = 2$, as suggested in [9]. These parameters have a marginal influence on the final loss estimate. Using this information, The previous equation can be solved to determine the entropy increase due to mixing $\Delta s = s_{\text{mix}} - s_a$ and the deviation angle δ .

- **Shock Loss.** When the flow exceeds the speed of sound, shock waves are formed which generate an increase in entropy and reduce efficiency. Rankine-Hugoniot relations are used to estimate the changes in thermodynamic properties through the shock wave.

$$h_B - h_A = \frac{1}{2} (P_B - P_A) (\nu_A + \nu_B) \quad (2.24)$$

$$-\frac{P_B - P_A}{\nu_B - \nu_A} = (\rho_A V_A \sin \epsilon)^2 \quad (2.25)$$

$$\rho_A \tan \epsilon = \rho_B \tan(\epsilon - \delta) \quad (2.26)$$

$$V_A \cos \epsilon = V_B \cos(\epsilon - \delta) \quad (2.27)$$

Here ϵ represents the shock angle, δ is the deviation angle, while A and B correspond to the pre and post shock states, respectively. The shock angle is related to the output conditions of the cascade.

- **Endwall Loss.** They include the viscous dissipation in the boundary layers along the hub and case, as well as the mixing of secondary flows. Since secondary flows are complex, semi-empirical correlations are used to estimate these losses.

- **Tip-Leakage Loss.** They occur in unshrouded rotor blades due to flow escaping through the gap between the blade tip and the turbine case. The entropy produced is calculated as:

$$T\Delta s = \frac{1}{\dot{m}} \int V_{ss}^2 \left(1 - \frac{V_{ps}}{V_{ss}}\right) d\dot{m}_j \quad (2.28)$$

The discharge coefficient C_c takes on typical values between 0.3 and 0.4 for rotating blades and the infinitesimal leakage mass flow rate can be estimated as [8]:

$$d\dot{m}_j = C_{cu} g \sqrt{2\rho_{ps} (P_{ps} - P_{ss})} dz \quad (2.29)$$

2.2.4 Mean Line Analysis

The study cases can be described by the following quantities, included in the configuration files:

- Working Fluid = Air
- Reduced Pressure $P_r = 2.11$
- Reduced Temperature $T_r = 7.55$
- Loss components = active
- Leakage = Unshrouded
- $\alpha_0 = 0^\circ$
- Fixed ϕ along the stage
- 3D blade design methodology = Free Vortex

These quantities are the same for the three turbine stages, while there are two parameters that differ for each case: the expansion ratio β and the hub to tip radius ratio R_{hub}/R_{tip} .

The expansion ratios are estimated as explained in the paragraph 2.1, while the R_{hub}/R_{tip} parameter requires further analysis and consideration to determine a correct value, as this quantity influences many other factors, including the final dimensions.

Hub-to-Tip Radius Ratio

The hub-to-tip ratio is a crucial design parameter in axial-flow turbines, affecting several aspects of performance, efficiency and mechanical constraints. TurboSim recommends a default values of $R_{hub}/R_{tip} = 0.818181818182$ at stator outlet.

The hub-to-tip ratio influences:

- *Flow Path Configuration.* It defines the cross-sectional shape of the turbine annulus, affecting the velocity distribution and pressure gradients.
- *Blade Loading.* A smaller hub-to-shroud ratio leads to higher blade loading at the hub, potentially causing mechanical stresses and aerodynamic losses.
- *Efficiency.* The ratio influences the distribution of reaction across the annulus, which in turn affects total turbine efficiency.
- *Structural Considerations.* A lower hub-to-shroud ratio can lead to longer, more slender blades, which are more prone to bending and vibrational issues.

The selection of velocity diagram parameters is influenced by the turbine's design-point pressure ratio, primarily because it constrains the hub-to-tip ratio, which in turn affects the velocity diagram [10].

As stated in Ref. [10], the hub-to-tip radius ratio should be specified within a range of 0.6 to 0.875, at least for the expansion ratios considered in the study. The upper limit is primarily set to prevent excessive clearance and other annulus losses, while the lower limit is maintained to ensure adequate blade mounting and to address structural stress considerations.

More specifically, in the figure 2.6 the relationship between the hub-to-tip ratio and the design-point pressure ratio is illustrated. The variation of this parameter is presented for two boundary conditions: one assuming a constant shroud diameter and the other a constant hub diameter.

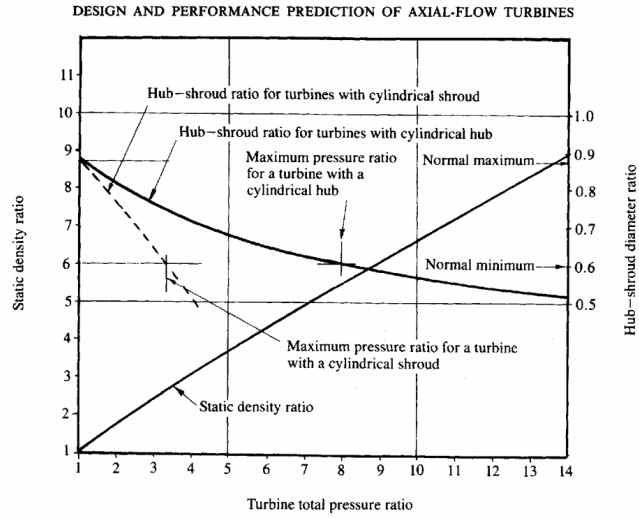


Figure 2.6: Variation of turbine static density ratio and hub-tip diameter ratio with pressure ratio [10].

The results indicate that a cylindrical shroud can be used for turbine pressure ratios up to approximately 3.0. For a constant hub diameter, the limiting pressure ratio is around 7.0, assuming a minimum allowable hub-to-tip ratio of 0.6. However, for higher pressure ratios, an increase in hub diameter is generally required, resulting in an increase in R_{hub}/R_{tip} .

Based on these considerations, it is possible to determine appropriate values for R_{hub}/R_{tip} .

The first turbine stage has an expansion ratio of less than 7, allowing the TurboSim default hub-to-tip ratio to be applied. In contrast, the second stage operates at a higher expansion ratio, requiring the application of the guidelines outlined in the referenced paper. As recommended, the hub-to-tip ratio is set to 0.875 to accommodate the increased expansion ratio and ensure optimal performance.

The third turbine has an expansion ratio ($\beta = 30$) completely out of the range considered in the previous paper. Therefore, based on Ref. [11], the hub-to-tip ratio is set to 0.9, as this value has been shown to reduce losses and improve turbine efficiency.

Thus, the final choices for each turbine are as follows:

1. $R_{hub}/R_{tip} = 0.8181818182$
2. $R_{hub}/R_{tip} = 0.875$
3. $R_{hub}/R_{tip} = 0.9$

Dimensional Parameters

Another key consideration is the dimensioning of the parameters, because TurboSim does not perform as it uses non-dimensional parameters. This is necessary in order to determine the blade heights, mean diameters and the rotational speeds.

In order to realise a complete mean line design, in many of the most important sources, such as in Ref. [7] and Ref. [12], it is mentioned that another input parameter is needed to dimension the parameters. This can be the mass flow rate, the output power required or the rotational speed. Therefore, in addition to TurboSim, a next step is needed to complete the preliminary design, which involves deciding on one of these parameters and subsequent relations.

It is more common to apply a mass flow rate and a typical value is $\dot{m} = 10\text{kg/s}$, as recommended by the open cycle, which requires a mass flow rate that is not excessively high.

Thus, the axial flow area is determined as in 2.30.

$$A_x = \frac{\dot{m}}{\rho\phi U} \approx 2\pi \times R_m H \quad (2.30)$$

Given H/R_m , the mean radius is calculated as in 2.31.

$$R_m = \sqrt{\frac{A_x}{2\pi \cdot \frac{H}{R_m}}} \quad (2.31)$$

As a consequence, all dimensional quantities, which TurboSim determines in a non-dimensional form, can be estimated: $H_0, H_1, H_2, H_3, R_t, R_h, D_m, \omega$.

Design Guidelines

The software gives the results computing maps as a function of the flow coefficient ϕ (2.32) and the total-to-static loading coefficient K_{is} (eq. 2.33).

$$\phi = \frac{V_m}{U_2} \quad (2.32)$$

$$K_{is} = \frac{h_{t,0} - h_{is,3}}{U_2^2} \quad (2.33)$$

K_{is} differs from the total-to-total loading coefficient ψ (2.34), which is commonly used in mean-line analysis. The former is considered to account for the non-ideal effects of the thermodynamic conditions involved in such studies.

$$\psi = \frac{h_{t,0} - h_{t,3}}{U_2^2} = \frac{U_2 V_{t,2} - U_3 V_{t,3}}{U_2^2} \quad (2.34)$$

To select the right combination of ϕ and K_{is} , a series of design guidelines are considered.

For single-stage configurations, a higher loading coefficient is generally preferred to maximise energy extraction in a limited number of components. In the mean-line design approach, the flow coefficient is selected based on efficiency maps, taking into account the degree of reaction and the loading coefficient [10].

Furthermore, the choice of efficiency depends on the stage configuration. In the case of a single stage, the series of total-to-static efficiency curves is generally more appropriate, as it provides a more accurate representation of actual performance considering the pressure drop across the stage. Conversely, for multi-stage designs, total-to-total efficiency is commonly used, which better captures the cumulative performance of the entire system, taking into account the interactions between multiple stages [7] [12].

Additionally, a set of recommendations is necessary to identify the best design:

- The axial Mach number should remain subsonic to maintain stable flow conditions.
- The stator flow angle should be in the range of 65° to 75° , typical of these kinds of turbines.
- The rotor flow angle should be minimized to reduce the amount of unused kinetic energy at rotor outlet.
- The rotor outlet absolute Mach number should also be subsonic to reduce kinetic losses downstream of the rotor and facilitate uniform downstream flow conditions.

2.2.5 Chosen Designs

Considering the guidelines and the TurboSim output maps, shown in Appendix A, the following design criteria must be met:

- The loading coefficient K_{is} should be high.
- The flow coefficient ϕ should be chosen to maximise efficiency.
- The stator outlet flow angle must be within the range of 65° - 75° .
- The target Mach numbers should be achieved.
- The peripheral speed must be high enough.

To facilitate a precise analysis of the Mach number at the rotor inlet, it is advantageous to select the same pair of design parameters ϕ and K_{is} while keeping $R = 0.25$ fixed. This approach allows for a clearer evaluation of the impact of this parameter as the expansion ratio varies across the three turbines. Consequently, the same combination of ϕ and K is adopted as the final parameter set for all turbines.

To choose the right pair of duty coefficients, the most restrictive turbine stage is examined: the third one ($\beta = 30$).

In particular, the peripheral speed at mid-span is plotted in the figure 2.7. In this case, it is important that the peripheral speed U is not too low, so K_{is} should not be more than 10 or 11. However, at the same time, as shown in figure 2.8 by reducing K_{is} , the Mach number that is reached at the rotor input decreases a lot compared to the chosen target of 1.3. Moreover, the parameter ϕ also cannot increase because otherwise the stator output angle α decreases too much and cannot be less than 65° .

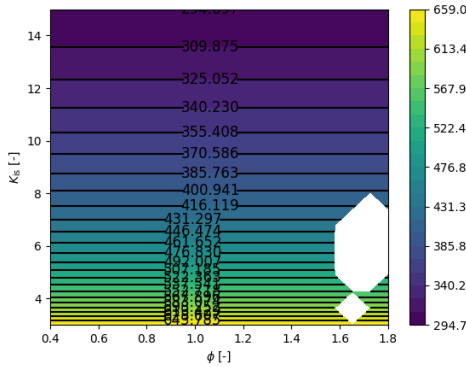


Figure 2.7: Peripheral speed at midspan

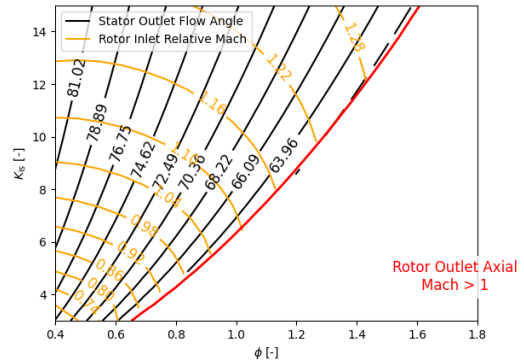


Figure 2.8: Stator Outlet flow angle

The design that best satisfies the various requirements is for the following pair of parameters: $\phi = 1.15$ and $K_{is} = 10$.

The characteristics for each turbine stage are presented in the table 2.1.

The final $Mach_{rel,rotor,inlet}$ deviates slightly from the expected value; however, these results are sufficiently reliable for analysis. Therefore, the study proceeds from this point to its conclusion.

	$\beta = 5$	$\beta = 16$	$\beta = 30$
$Mach_{rel,rotor,inlet}$	0.90	1.11	1.19
Ψ	3.354	3.163	3.085
η_{ts}	0.67	0.63	0.62
$\alpha_{out,stator} [^\circ]$	65.17	65.17	65.17
$\alpha_{out,rotor} [^\circ]$	-39.16	-37.71	-37.14
$Mach_{Ax,stator,outlet}$	0.56	0.70	0.76
$Mach_{Ax,rotor,outlet}$	0.62	0.80	0.88
$Mach_{Abs,stator,outlet}$	1.33	1.67	1.80
$Mach_{Abs,rotor,outlet}$	0.80	1.01	1.10
$U_{mid} [m/s]$	277.04	338.34	360.93
$U_{tip} [m/s]$	317.60	380.57	422.11

Table 2.1: Design Characteristics

The final results of the three chosen stages are expressed in the following figures.

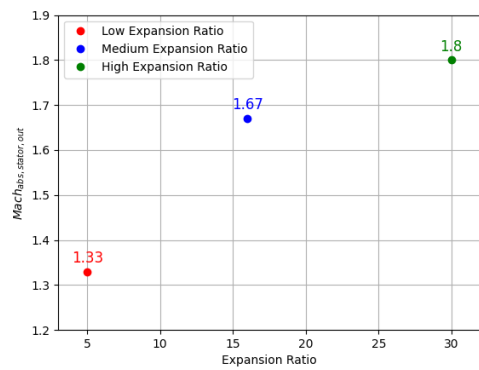
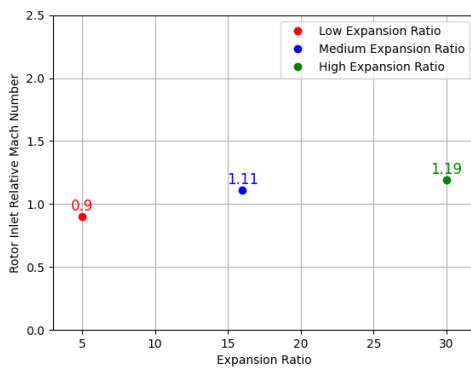


Figure 2.9: Mach numbers at rotor inlet **Figure 2.10:** Stator Outlet Mach numbers

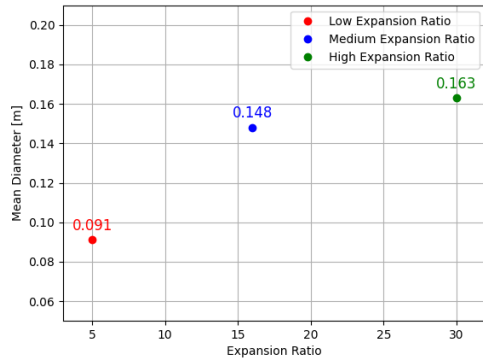


Figure 2.11: Mean diameters

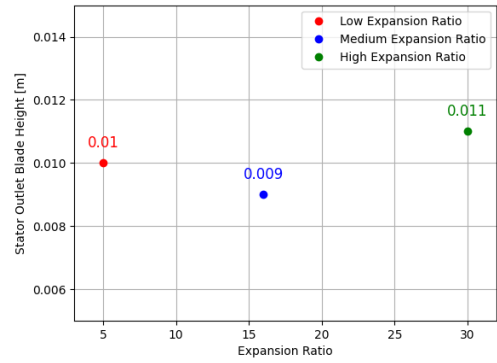


Figure 2.12: Heights at Stator Outlet

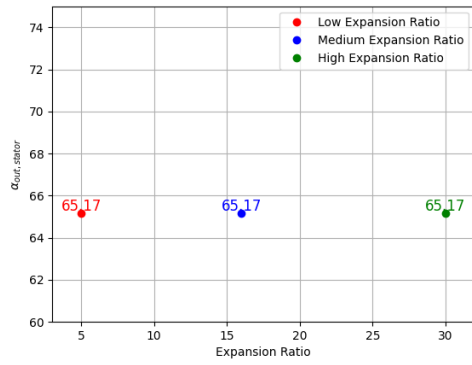


Figure 2.13: α at stator outlet

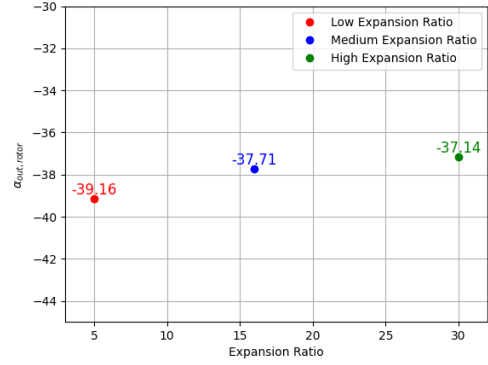


Figure 2.14: α at rotor outlet

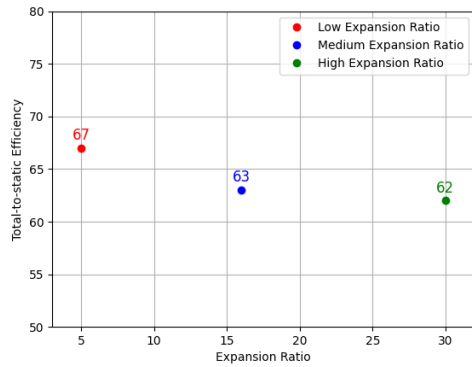


Figure 2.15: Total-to-static efficiency

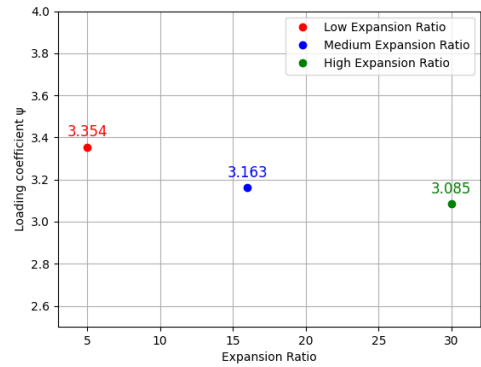


Figure 2.16: Loading Coefficient ψ

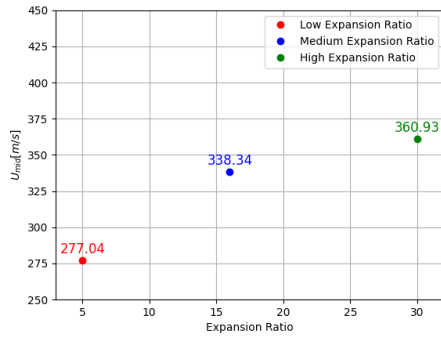


Figure 2.17: Peripheral velocities at midspan

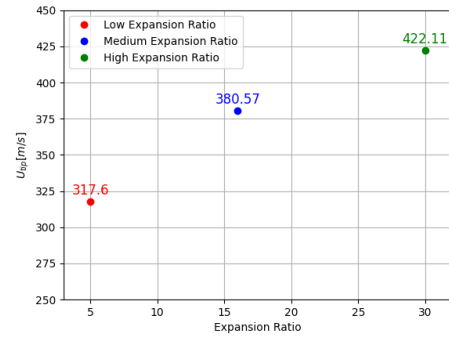


Figure 2.18: Peripheral velocities at tip

Consequently, the velocity triangles are as follows:

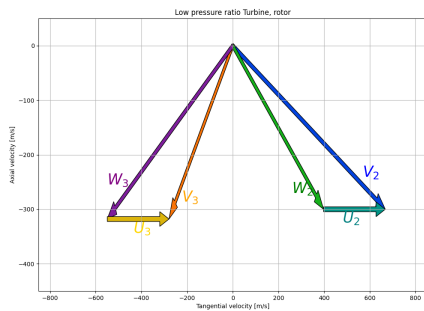


Figure 2.19: Low β stage, velocity triangle

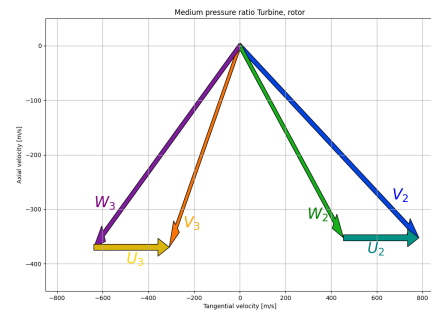


Figure 2.20: Medium β stage, velocity triangle

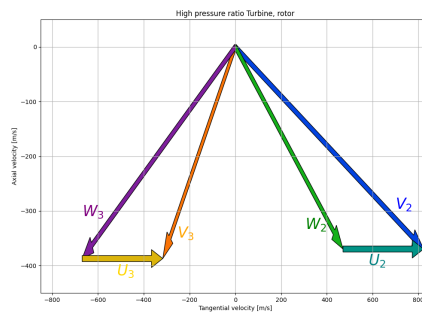


Figure 2.21: High β stage, velocity triangle

Once the mean line design is completed, the next step is to develop a method for constructing the stator and rotor blades. This involves translating the velocity triangles into a blade geometry that optimally aligns with the flow conditions.

Chapter 3

Blade Design

3.1 Method of Characteristics

In fluid dynamics, compressible flows play a crucial role, especially in machines such as turbines. When the velocity of a fluid reaches values comparable to or greater than the speed of sound, compressibility effects become dominant and the equations describing fluid motion take on a particular form.

One of the fundamental models for describing these phenomena are the Euler equations, which express the conservation of mass, momentum and energy by considering only convective flows, since in CFD convective and diffusive flows are considered separately. Mathematically, these equations are expressed as a system of partial differential equations in a conservative form (3.1) [13].

$$\left\{ \begin{array}{l} \frac{\partial \rho u}{\partial x} + \frac{\partial \rho v}{\partial y} = 0 \\ \frac{\partial}{\partial x} (\rho u^2 + p) + \frac{\partial}{\partial y} (\rho uv) = 0 \\ \frac{\partial}{\partial x} (\rho uv) + \frac{\partial}{\partial y} (\rho v^2 + p) = 0 \\ \frac{\partial}{\partial x} [u(p + \rho E)] + \frac{\partial}{\partial y} [v(p + \rho E)] = 0 \end{array} \right. \quad (3.1)$$

These equations are 2D, steady and hyperbolic. The latter means that information in the flow domain propagates along certain curves, called characteristics, and that the system can be solved by downstream methods, since each point in the flow depends only on upstream regions.

In contrast, in subsonic flows the system is elliptical, which implies that information propagates in all directions and that the solution at one point is influenced by the entire domain.

This distinction is particularly important when designing nozzles, turbines or

other aerodynamic components that operate at high speeds.

To solve hyperbolic equations in supersonic flows, one of the most accurate methods is the Method of Characteristics (MOC) [14]. This approach transforms a system of partial differential equations into a set of ordinary differential equations along specific curves known as characteristic lines. As the most precise marching-type technique for solving quasi-linear hyperbolic partial differential equations (PDE), the MOC reformulates the governing PDE into two fundamental equations: the characteristic equation and the compatibility equation. The characteristic equation determines the slope of the lines along which disturbances propagate, offering a structured framework for analysing and solving hyperbolic systems efficiently.

To better understand the concept of characteristics, it can be examined from both a physical and mathematical perspective, as elaborated in [15]:

- *Mathematical Interpretation:* a characteristic is a curve along which a physical property remains continuous, while its derivative may or may not be discontinuous. Along a characteristic curve, the governing partial differential equation can be transformed into an ordinary differential equation, significantly simplifying the problem.
- *Physical Interpretation:* a characteristic line represents the propagation path of physical disturbances, across which physical properties exhibit gradients and along which waves and signals travel in a compressible fluid. For instance, in supersonic flow fields, discontinuities propagate along Mach lines, making these lines the characteristics of the supersonic flow field.

The 2D Euler equations in their steady and conservative form are:

$$\frac{\partial}{\partial x} \begin{bmatrix} \rho u \\ \rho u^2 + p \\ \rho uv \\ u(\rho E + p) \end{bmatrix} + \frac{\partial}{\partial y} \begin{bmatrix} \rho v \\ \rho uv \\ \rho v^2 + p \\ v(\rho E + p) \end{bmatrix} = 0 \quad (3.2)$$

The non-conservative form using primitive-variable is:

$$A' \frac{\partial}{\partial x} \begin{bmatrix} a \\ u \\ s \end{bmatrix} + B' \frac{\partial}{\partial y} \begin{bmatrix} a \\ u \\ s \end{bmatrix} = 0 \quad (3.3)$$

with

$$A' = \begin{bmatrix} u & \delta a & 0 \\ \frac{a}{\delta} & u & -\frac{a^2}{\gamma R} \\ 0 & 0 & u \end{bmatrix}, \quad B' = \begin{bmatrix} v & \delta a & 0 \\ \frac{a}{\delta} & v & -\frac{a^2}{\gamma R} \\ 0 & 0 & v \end{bmatrix}$$

To study the hyperbolic nature of the Euler equations, the diagonalised system is:

$$\Lambda_x \frac{\partial}{\partial x} \begin{pmatrix} \omega_1 \\ \omega_2 \\ \omega_3 \end{pmatrix} + \Lambda_y \frac{\partial}{\partial y} \begin{pmatrix} \omega_1 \\ \omega_2 \\ \omega_3 \end{pmatrix} = 0 \quad (3.4)$$

$$\begin{bmatrix} \lambda_1^{(x)} & 0 & 0 \\ 0 & \lambda_2^{(x)} & 0 \\ 0 & 0 & \lambda_3^{(x)} \end{bmatrix} \frac{\partial}{\partial x} \begin{pmatrix} \omega_1 \\ \omega_2 \\ \omega_3 \end{pmatrix} + \begin{bmatrix} \lambda_1^{(y)} & 0 & 0 \\ 0 & \lambda_2^{(y)} & 0 \\ 0 & 0 & \lambda_3^{(y)} \end{bmatrix} \frac{\partial}{\partial y} \begin{pmatrix} \omega_1 \\ \omega_2 \\ \omega_3 \end{pmatrix} = 0 \quad (3.5)$$

where w_i are the characteristic variables.

The eigenvalues of the Jacobian matrix are found by solving the eigenvalue problem.

$$\det(A' - \lambda I) = 0. \quad (3.6)$$

The eigenvalues are as follows.

In the x -direction:

$$\lambda_1^{(x)} = u - a, \quad \lambda_2^{(x)} = u, \quad \lambda_3^{(x)} = u + a$$

In the y -direction:

$$\lambda_1^{(y)} = v - a, \quad \lambda_2^{(y)} = v, \quad \lambda_3^{(y)} = v + a$$

To find the characteristic variables in the 2D steady case, the generalized equations for the eigenvectors include the components dx and dy :

$$\begin{cases} d\omega_1 = \left(\frac{da}{\delta} - du - \frac{a}{\gamma R} ds \right) \cdot dx \\ d\omega_2 = ds \cdot dx \\ d\omega_3 = \left(-\frac{da}{\delta} + du - \frac{a}{\gamma R} ds \right) \cdot dx \end{cases}$$

and analogously for dy .

In 2D, the characteristic curves lie in the (x, y) plane and are tangential to the vector field associated with the eigenvalues (oblique characteristics). The compatibility equation is written in integral form as follows:

$$\int_{\text{characteristic}_i} d\omega_i = 0 \quad \text{for } i = 1, 2, 3$$

3.2 Supersonic Stator

The stator nozzle consists of three distinct sections: a converging section operating in the subsonic regime, a diverging section where the flow becomes supersonic and a straight section along the suction surface. The converging section accelerates the flow to sonic conditions and can be designed following the MOC. To minimize losses, this section is specifically shaped to achieve the full turning of the flow. The diverging section further accelerates the flow to reach the desired free-stream Mach number at the outlet and its design is based on the MOC, as previously discussed. Finally, the straight section on the suction surface has a length determined by the required nozzle angle [2].

The method of characteristics can be applied to the convergent-divergent nozzle section of the stator. As described in [2], a supersonic nozzle designed to produce a uniform and parallel flow is specifically shaped to ensure the correct expansion and subsequent redirection of the flow, as in figure 3.1.

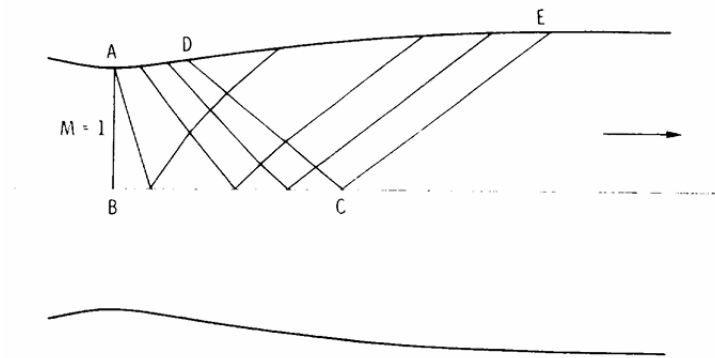


Figure 3.1: Supersonic nozzle [2]

The nozzle wall profile has two main curvatures:

- *AD segment.* The nozzle wall expands outward, allowing the flow to accelerate to supersonic speeds.
- *DE segment.* The wall curves inward again to restore the flow direction to its original orientation.

Point *D* represents the location where the wall reaches its maximum inclination. It is assumed that at the nozzle throat, the flow is sonic ($M = 1$), uniform and parallel.

Since the nozzle is symmetrical, its central axis can be treated as a line of symmetry, which can be replaced by a solid boundary in simulations and design

analyses. This approach reduces computational effort by focusing only on one half of the nozzle.

The region $ABCD$ is defined as *expansion zone*. The curved wall AD generates expansion waves that propagate and subsequently reflect off the central axis of the nozzle.

This process allows for further acceleration of the flow, which makes it supersonic. The expansion waves originate due to the wall curvature and are necessary to ensure the proper expansion of the flow, reaching the desired velocity and pressure downstream.

The region $DCED$ is called *straightening section*. Here, the wall is curved in such a way that the incoming expansion waves are cancelled out. The wave cancellation method follows the principles of elementary flow solutions.

Beyond the CE section, the flow is parallel, uniform and supersonic, making it ready to exit the nozzle. The outlet Mach number depends on the amount of flow expansion that occurs in the AD section.

If the pressure difference is high, the expansion will be greater, resulting in a higher final Mach number. For very high Mach numbers, the nozzle may become excessively long, making it impractical for applications such as supersonic turbines. In such cases, an optimized nozzle design is implemented, maintaining the desired effects while reducing the overall length, but in this project the MOC is still used.

The design process involves two primary steps: first, the divergent section of the supersonic stator is developed using the MOC and then the blade shape is generated through a geometric transformation [14].

3.2.1 Nozzle Design

To design the convergent-divergent section, an internally developed tool from TU Delft is employed. As explained in [14], the MOC is applied to design the divergent section of the supersonic nozzle under the assumption of steady homentropic flow. Such a flow is governed by the two-dimensional isentropic Euler equations.

To initialise the calculation, it is necessary to determine the sonic line, i.e., the line along which the Mach number is exactly $M = 1$. This is the starting point for the analysis of expansive waves that accelerate the flow beyond Mach 1.

The divergent section of the diffuser is divided into two regions:

- *Kernel region*, is the first part after the nozzle throat and is defined by imposing a circular radius connecting the throat to the point from which the expansion wave starts. This expansion wave accelerates the flow to the desired Mach value along the nozzle axis.
- *Reflex region*, which follows the kernel region and is designed to conserve mass and ensure uniform outlet conditions. It redirects the flow to reduce

inhomogeneities.

To calculate the velocity and flow conditions at each point along the expansion, two equations from the family of characteristic and compatibility equations are solved:

$$\lambda_{\pm} = \tan(\phi \pm \alpha) \quad (3.7)$$

$$(u^2 - c^2) du_{\pm} + (v^2 - c^2)\lambda_{\pm}^{-1} dv_{\pm} = 0 \quad (3.8)$$

Here, the subscripts + and - represent the two families of characteristic lines, while λ is the characteristic slope, ϕ is the flow angle, α is the Mach angle, c is the speed of sound and u and v are the velocities in the x and y directions [14].

From the sonic line, the position of the next point in the kernel or reflex region is determined using the characteristic equation. Specifically, this equation defines the direction of a pressure wave at a given point, with two waves starting at each point, with slopes of opposite sign. By intersecting the characteristic waves originating from two adjacent points, the coordinates (x,y) of a new point are obtained. The compatibility equation for these intersecting waves is then solved simultaneously to determine the velocity components (u,v) at the new point. At this point, the speed of sound, entropy and enthalpy are calculated using an appropriate equation of state:

$$c = c(H, s) \quad (3.9)$$

$$s = s(P_{\text{tot}}, T_{\text{tot}}) \quad (3.10)$$

$$H = H(V, H_{\text{tot}}) = H_{\text{tot}}(P_{\text{tot}}, T_{\text{tot}}) - \frac{V^2}{2} \quad (3.11)$$

The Mach and flow angles are as follows:

$$\alpha = \arcsin\left(\frac{1}{M}\right) \quad (3.12)$$

$$\phi = \arctan\left(\frac{v}{u}\right) \quad (3.13)$$

The result of this process is shown in figure 3.2, where the lines with positive slope represent positive characteristics and those with negative slope are negative characteristic lines.

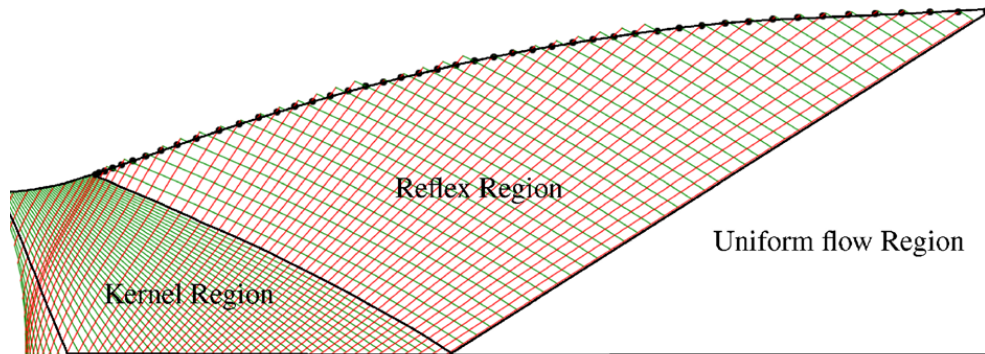


Figure 3.2: Method of characteristics implemented to design the divergent section of the supersonic nozzle [14]

To account for non-ideal fluid effects, the multi-parameter equation of state of Span and Wagner [16] is used to calculate the thermodynamic quantities and consequently the shape of the divergent part depends on the thermodynamics of the points where the expansion takes place and on the working fluid. In the case of air, the nozzle is typically shorter and smaller compared to other more complex fluid.

The tool used, which is based on this procedure, is the MOC tool from OpenMOC. This tool requires a number of inputs to function, which are derived from the previous results of TurboSim. At the same time, however, there is one parameter that must be paid more attention to, which is the absolute Mach number of the stator output.

The Mach number at the stator outlet differs from the value provided by TurboSim because the latter does not consider a stator designed as a convergent-divergent nozzle; instead, it directly provides the Mach number after post-expansion. In contrast, OpenMOC requires the Mach number prior to post-expansion.

To ensure compatibility with OpenMOC, the Mach numbers from TurboSim are adjusted proportionally to account for post-expansion effects.

The issue is to figure out the correct value of this post-expansion and consequently apply it to the stator outlet Mach number. A previous study, conducted using the same software, analysed the post-expansion ratio and its dependence on the expansion ratio and on the working fluid, as explained in the reference [17]. Specifically, the authors investigated the optimal value of the post-expansion ratio by varying the working fluid, keeping the design parameters constant, and then varying the design parameters for a same working fluid. The interesting results can be explained by figures 3.3 and 3.4.

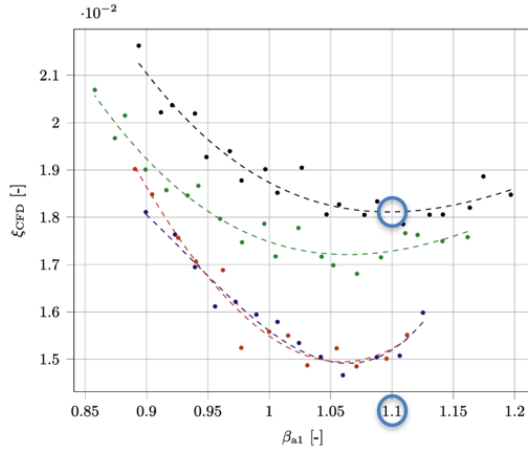


Figure 3.3: Peripheral speed at midspan [17]

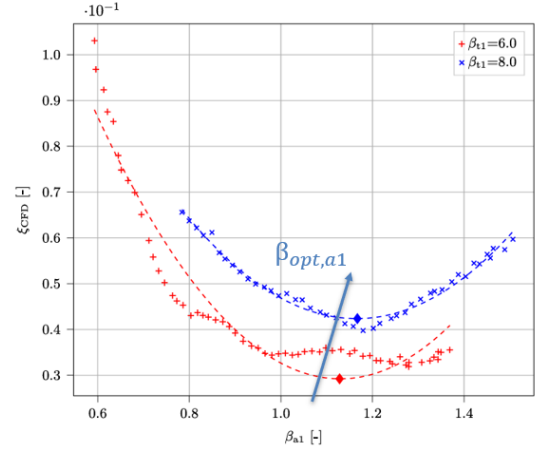


Figure 3.4: Stator Outlet flow angle [17]

Figure 3.3 shows the variation of the total losses ξ with a post-expansion ratio (β_{a1}) for vanes operating with an expansion ratio $\beta = 6$, a flow angle $\phi_a = 70^\circ$ and solidity $\sigma = 1$ and for different working fluids. The dots represent the values obtained from CFD simulations at discrete intervals of β_{a1} and the dashed lines are trend lines obtained by fitting the data points with a cubic functional form.

The black dashed line is representative of air and the value of a post-expansion that minimizes losses is about $\beta_{a1}=1.1$.

Figure 3.3 is also an important reference because it shows the influence of the expansion ratio on the optimal post-expansion value. A higher expansion ratio means higher losses, as the Mach number increases in the flow channel. In fact, for higher values of β , the optimal post-expansion value is a single value due to the stronger shock wave, which leads to a higher sensitivity of the overall losses. On the contrary, for lower β values, the minimum losses are reached for a series of post-expansion values. Consequently, the optimum value rises as the expansion ratio increases.

The final selected values are:

- In the first case, the post-expansion ratio is 6% of the total expansion ratio.
- In the second case, it is 9%.
- In the third case, it is 10%.

The Mach number is selected proportionally to these values, as stated in the table 3.1.

	TurboSim $M_{\text{stator,out}}$	OpenMOC $M_{\text{stator,out}}$	Post-Expansion
$\beta = 5$	1.33	1.27	6%
$\beta = 16$	1.65	1.50	9%
$\beta = 30$	1.80	1.62	10%

Table 3.1: Comparison of TurboSim and OpenMOC stator outlet Mach numbers for different expansion ratios.

The MOC tool computed the results illustrated in figures 3.5, 3.6 and 3.7.

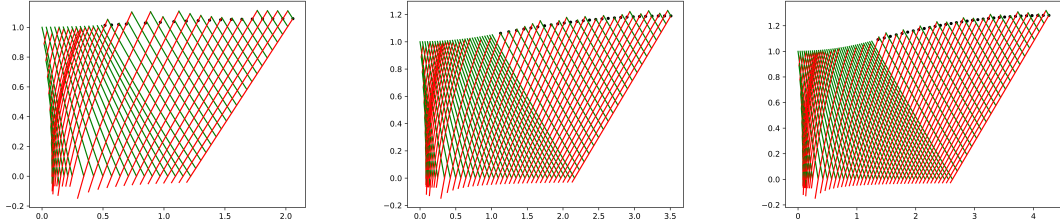


Figure 3.5: Divergent section of the low expansion ratio vane **Figure 3.6:** Divergent section of the medium expansion ratio vane **Figure 3.7:** Divergent section of the high expansion ratio vane

3.2.2 Axial Stator Design

The divergent section is integrated into the overall nozzle design. To develop the supersonic stator, another OpenMOC tool is used. This tool was originally designed for radial stators, as detailed in [14], and is then modified to accommodate the axial configuration.

An important challenge is designing the pressure side to ensure that the throat is positioned correctly. This is then validated through CFD analysis by verifying that the sonic line is indeed located at the throat. Additionally, it is crucial to prevent excessive acceleration of the flow before reaching the throat, as this could lead to premature supersonic conditions. To mitigate this risk, the leading edge should be thickened using a similar procedure to the one described in reference [18].

After implementing all the necessary modifications to meet the specified requirements, the final results are presented in figures 3.8, 3.9, 3.10 for the vanes at low, medium and high pressure ratios.

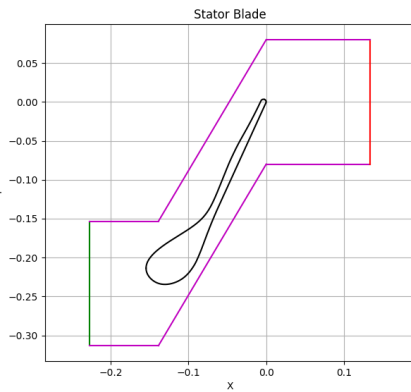


Figure 3.8: Stator Blade of the low pressure ratio turbine

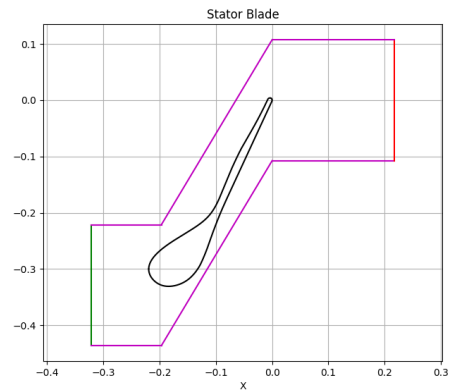


Figure 3.9: Stator Blade of the medium pressure ratio turbine

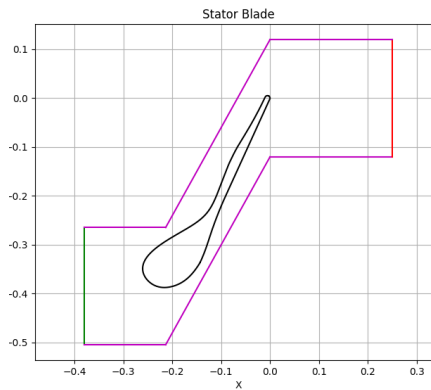


Figure 3.10: Stator Blade of the high pressure ratio turbine

3.3 Supersonic rotor

In the supersonic rotor blade design, flow deflection is achieved through a vortex-type velocity distribution in the concentric circular arc section. This distribution is realised through transition arcs, the design of which is based on Prandtl-Meyer angles. However, this method is not flexible in including external effects such as body forces and is not adequate for the typical operating conditions where dense gas effects significantly influence the efficiency of the vane geometry [19].

These effects are considered in another tool implemented in OpenMOC. The authors of this tool aimed to address the previous limitations by eliminating the use of Prandtl-Meyer angles and instead applying the MOC directly to the compatibility

equation, as explained in reference [19].

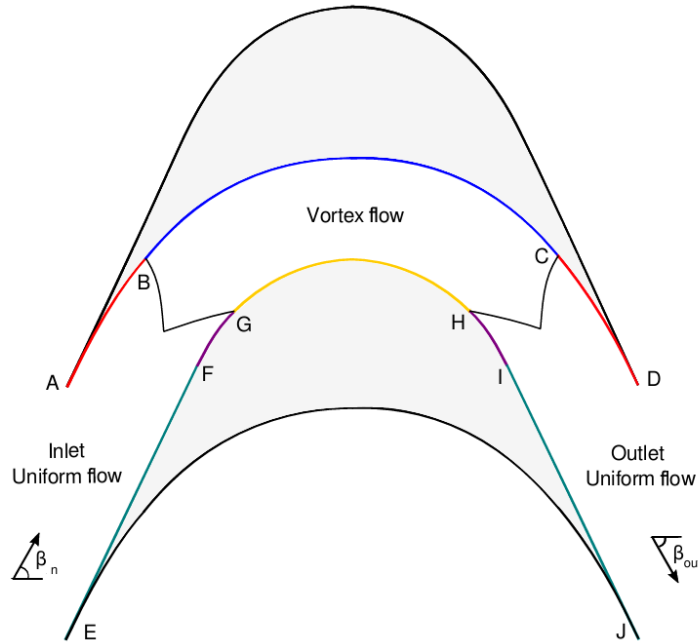


Figure 3.11: Supersonic axial rotor blade sections [19]

The concept focuses on enabling a smooth supersonic flow passage between two concentric circles, allowing for significant turning of the fluid without generating local shocks. To accomplish this, the blade design is structured into three key sections: the inlet transition arc, which gradually converts the uniform supersonic inflow into a vortex-type flow; the concentric circular arc section, which sustains the vortex flow while redirecting it; and the outlet transition arc, which transitions the vortex flow back to uniform conditions at the blade exit, as shown in Figure 3.11.

Given the inlet relative flow angle, inlet and outlet Mach numbers, the code generates a rotor profile. The input Mach number must be supersonic for the software to work, so this tool cannot be applied to the first stage of the turbine, which has a subsonic relative rotor input Mach number. Instead, it is only applied to the second and third stages.

The blade geometries, together with the boundaries for the CFD simulations, are shown in figures 3.12 and 3.13.

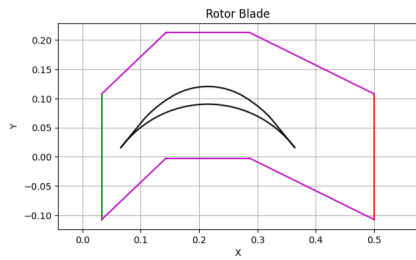


Figure 3.12: Rotor blade of the medium pressure ratio turbine

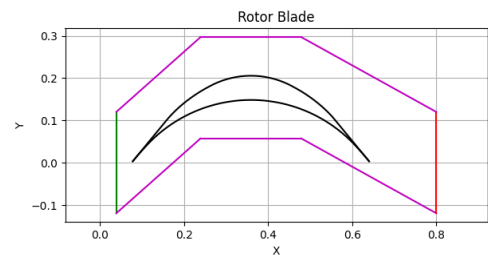


Figure 3.13: Rotor blade of the high pressure ratio turbine

The x and y coordinates in figures are in the dimensional form (m). However, the tool gives results in a dimensionless form, so the dimensions are scaled in order to obtain the same axial chord and pitch as the TurboSim outputs, with a solidity of 0.72 for the second rotor and 0.62 for the third one.

As for the domains, they are constructed based on the pitch. For the second stator, the same pitch as the mean line is used, since its value matches that of the stator. For the third rotor, the pitch is adjusted to match the pitch of the corresponding stator, to ensure compatibility with unsteady simulations.

Chapter 4

Computational Fluid Dynamics of Supersonic Turbines

4.1 Flow Field in Supersonic Turbines

Fluid dynamics analysis is a fundamental aspect of turbine design, particularly for stages operating in supersonic conditions where the presence of shock waves, separation phenomena and strong pressure gradients makes predicting flow behaviour complex. In this context, computational fluid dynamics is an essential tool for understanding and optimising turbine performance; indeed, many modern design methods are based on CFD optimisation which allows for losses reduction.

CFD allows the Navier-Stokes equations to be solved numerically, providing a detailed description of the flow field and enabling accurate prediction of system performance.

Supersonic turbines are characterised by a complex interaction between the stator and rotor blades, in which the highly compressible flow generates shock waves and expansion fans. A key feature of these turbines is the formation of shock waves at the trailing edge of the stator, which impact the rotor, affecting its efficiency [18]. Figure 4.1 shows a simulation of the static pressure field in a supersonic turbine. On the left, the pressure distribution along the rows of blades can be observed. On the right, the focus is on the characteristic wave system of the flow through the turbine blades. Oblique shock waves (in blue), which form at the outlet of the stator vanes and interact with the flow along the rotor, can be clearly distinguished. In addition, there are detached shock waves, or bow shocks (in red), which develop due to the interaction between the supersonic flow and the

blade geometry.

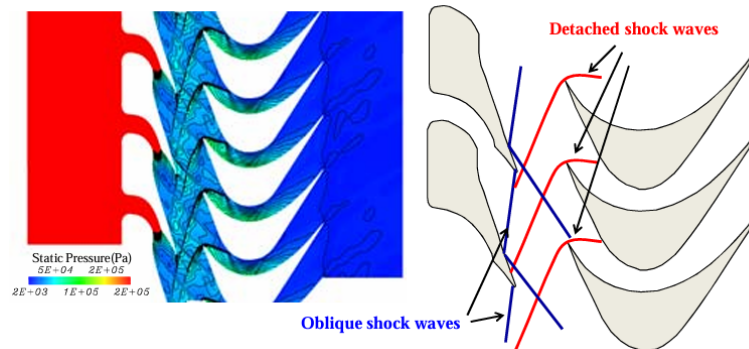


Figure 4.1: Static pressure contours and schematic of shock waves [20]

In the region of stator-rotor interaction, pressure waves can move upstream through the subsonic flow near the pressure surface of the adjacent rotor, strengthening when they reach the supersonic flow [21]. This phenomenon contributes to significant fluctuations in Mach number, pressure and aerodynamic forces on the rotor. In addition, the geometry of the rotor leading edge can influence the non-uniformity of the downstream flow, leading to variations in turbulence and boundary layer separation [22].

Another critical aspect involves the interaction between shock waves and the pressure field. At high Mach numbers at the stator vane outlet, the main source of excitation is the shock system formed at the trailing edge of the vane [23]. This system generates an increase in forces and torques on the rotor blades, with effects amplified by the rise in the pressure ratio in the turbine.

Furthermore, the pressure ratio in the stage affects the position and inclination of the shock wave at the trailing edge of the vane, shifting its impact downstream and modifying the Mach number in the rear regions. This contributes to the generation of reflected waves and the creation of boundary layer separation zones [23].

The main approaches commonly employed to analyse the interaction between stator and rotor blade rows are steady-state analyses, for example, implementing a mixing plane, and unsteady simulations.

The mixing plane approach consists of averaging the momentum field between the stator and rotor, eliminating phase variations and transient instabilities. The flow field is averaged along the circumferential direction, making the approach particularly suitable for obtaining time-averaged results at low computational cost [20]. However, this model shows an increase in pressure due to the influence of the shock waves detached from the adjacent rotor vane. In addition, an increase

in the Mach number at the stator inlet is observed, leading to the generation of oblique shock waves which, reflected on the stator walls, impact the rotor inlet. As a result, the field of motion between the nozzle outlet and the rotor inlet becomes highly complex, characterised by reflections and interference between shock waves. Therefore, the use of the mixing plane in supersonic turbines can lead to an overestimation of losses due to shock waves and stator-rotor interaction [24].

On the other hand, unsteady simulations allow pressure fluctuations and transient aerodynamic interactions to be resolved directly. This approach makes it possible to capture effects such as shock wave propagation, oscillations of aerodynamic forces on the blades and the variation of the flow field over time.

One of the most interesting aspects of the unsteady simulations is the significant difference from the steady results for the same flow condition, as shown in the reference [24]. In fact, the flow non-uniformity along the circumferential direction at the trailing edge of the vane is much more pronounced in the unsteady simulations than in the steady ones, with variations of more than 40% under the most unfavourable conditions [21]. A further advantage lies in their ability to highlight the role of stator vanes wakes. The wakes generate a modulation of the pressure field that helps to dampen the pressure gradients associated with the reflected waves, thus reducing flow instability [24].

4.2 Navier-Stokes Equations

Computational fluid dynamics uses numerical techniques and computational methods to solve fluid flow problems, in particular the Navier-Stokes (NS) equations, which can be formulated in different ways. The compressible forms of these equations are shown in 4.1.

$$\begin{cases} \frac{\partial \rho}{\partial t} + \nabla \cdot (\rho \vec{q}) = 0 \\ \frac{\partial(\rho \vec{q})}{\partial t} + \nabla \cdot (\rho \vec{q} \vec{q}) = \nabla \cdot [\sigma] + \rho \vec{f}_e \\ \frac{\partial \rho E}{\partial t} + \nabla \cdot (\rho \vec{q} E) = \nabla \cdot ((-p\mathbb{I} + [\tau]) \vec{q}) + \rho \vec{f}_e \cdot \vec{q} - \nabla \cdot \vec{q}_T \end{cases} \quad (4.1)$$

ρ is the density, \vec{q} is the velocity vector, E is the total energy, $\sigma = -p\mathbb{I} + [\tau]$ represents the stress tensor, \vec{f}_e is an external force term (such as Coriolis or centrifugal force), p is the pressure, \mathbb{I} is the identity matrix, $[\tau]$ is the viscous stress tensor and \vec{q}_T is the heat flux. In compact form, the compressible Navier-Stokes equations can be written as in 4.2.

$$\frac{\partial}{\partial t} \begin{Bmatrix} \rho \\ \rho \vec{q} \\ \rho E \end{Bmatrix} + \nabla \cdot \begin{Bmatrix} \rho \vec{q} \\ \rho \vec{q} \vec{q} - p \mathbb{I} + [\tau] \\ (\rho E + p) \vec{q} - [\tau] \vec{q} - k \nabla T \end{Bmatrix} = \begin{Bmatrix} 0 \\ \rho \vec{f}_e \\ \rho \vec{f}_e \cdot \vec{q} \end{Bmatrix} \quad (4.2)$$

4.3 Turbulence Modelling

Turbulent flow is an unsteady, three-dimensional phenomenon characterized by a series of vortical structures that evolve and progressively break down into smaller vortices. This makes it a multi-scale problem: the largest eddies, which are approximately the size of the body being studied, tend to break down transferring energy to progressively smaller scales until reaching the dissipative scales. This process is known as the turbulent energy cascade. The largest vortices, known as integral length scales, are strongly influenced by the local geometry and flow system, whereas the smallest vortices, near the Kolmogorov scale η , exhibit more universal characteristics. The ratio between the largest and smallest turbulence structures increases with the Reynolds number, leading to a wide range of interacting scales. The characteristic time associated with large eddies is approximately $t = L/U_0$, where L is the characteristic length of the system and U_0 is the characteristic velocity. The Kolmogorov time scale, on the other hand, can be estimated as $\sqrt{\mu/\rho\epsilon}$, where ϵ is the viscous dissipation [25].

To handle the complexity of turbulence, most modelling approaches employ some form of averaging, which can be temporal, spatial or a combination of both. This allows for a reduction in computational cost while providing a feasible description of the flow.

There are three main approaches to numerical turbulence simulation [13]:

- **Direct Numerical Simulations (DNS)**: directly solve the Navier-Stokes equations without turbulence models, integrating with a spatial and temporal grid fine enough to capture all turbulent determines the spatial resolution Δx , while the total number of cells depends on the size of the problem (determined by the largest eddies). The number of grid cells increases with the Reynolds number because the ratio between the largest and smallest vortices grows. Additionally, due to the Courant-Friedrichs-Lewy (CFL) condition, smaller cells require smaller time steps. The computational cost of DNS scales approximately as $\mathcal{O}(Re^3)$.
- **Large Eddy Simulations (LES)**: solve the larger turbulent scales directly, while the smaller scales, which are typically more universal, are modelled using a sub-grid scale model. The separation between resolved and unresolved scales is typically determined by a filter, which is often chosen to be proportional to

the grid resolution. Sub-grid scale models introduce their effects on the larger (resolved) scales. These models aim to represent how the unresolved turbulence interacts with the resolved flow structures. It is used until $Re \approx 10^5$.

- **Reynolds-Averaged Navier-Stokes (RANS)**: Averages the equations over time or space to obtain a mean field, fully modelling the turbulence. It is used for high Reynolds numbers.

RANS are obtained by decomposing the solution into mean value and fluctuation:

$$u_i = \bar{u}_i + u'_i \quad (4.3)$$

This decomposition introduces the Reynolds stress tensor, which represents the effect of turbulent fluctuations on the mean field:

$$-\rho \overline{u'_i u'_j} \quad (4.4)$$

The mean value can be calculated in different ways, depending on the nature of the problem [13]:

- *Statistically steady problems*. Time average:

$$\bar{u}_i(x) = \lim_{T \rightarrow \infty} \frac{1}{T} \int_t^{t+T} u_i(x, t) dt$$

- *Homogeneous turbulence problems*. Spatial average:

$$\bar{u}_i(t) = \lim_{\Omega \rightarrow \infty} \frac{1}{\Omega} \int_{\Omega} u_i(x, t) d\Omega$$

- *Generic Problem*. Overall average:

$$\bar{u}_i(x, t) = \lim_{N \rightarrow \infty} \frac{1}{N} \sum_{i=1}^N u_i(x, t)$$

- *Compressible Flow Problems*. In this case, the Favre averaging is implemented, where $\bar{\rho}$ is the mean density computed using one of the previous approaches, while $\tilde{u}_i(x)$ is the Favre average, given by:

$$\tilde{u}_i(x) = \frac{1}{\bar{\rho}} \lim_{T \rightarrow \infty} \int_t^{t+T} \rho u_i(x, t) dt$$

Thus, the solution will be:

$$u_i(x, t) = \tilde{u}_i(x) + U_i''$$

where U_i'' is the fluctuation averaged by Favre.

In compressible RANS (Favre-averaged Navier-Stokes equations), density and pressure are Reynolds-averaged, while all other variables are Favre-averaged.

It results:

$$\frac{\partial \bar{\rho}}{\partial t} + \frac{\partial}{\partial x_i}(\bar{\rho} \tilde{q}_i) = 0 \quad (4.5)$$

$$\frac{\partial}{\partial t}(\bar{\rho} \tilde{q}_i) + \frac{\partial}{\partial x_j}(\bar{\rho} \tilde{q}_i \tilde{q}_j) = -\frac{\partial \bar{p}}{\partial x_i} + \frac{\partial}{\partial x_j}(\bar{\tau}_{ij} - \bar{\rho} \tilde{q}_i'' \tilde{q}_j'') \quad (4.6)$$

In equation 4.6, the term $\tau_{ij}^F = -\bar{\rho} \tilde{q}_i'' \tilde{q}_j''$ is the Reynolds stress tensor obtained by Favre averaging.

The Boussinesq hypothesis assumes that the τ_{ij}^F stresses are proportional to the mean velocity gradient, as in equation 4.7.

$$\bar{\tau}_{ij}^F = 2\mu_t \tilde{S}_{ij} - \frac{2}{3}\mu_t \frac{\partial \tilde{q}_k}{\partial x_k} \delta_{ij} - \frac{2}{3}\bar{\rho} k \delta_{ij} \quad (4.7)$$

Where:

- $\tilde{S}_{ij} = \frac{1}{2} \left(\frac{\partial \tilde{q}_i}{\partial x_j} + \frac{\partial \tilde{q}_j}{\partial x_i} \right)$ is the strain rate tensor.
- k is the turbulent kinetic energy.
- μ_t is the eddy viscosity, which accounts for the fluctuations at the turbulent scales that describe the velocity gradient of molecules diffusing in both directions. Therefore, it perceives a gradient in the mean field associated with the momentum exchange.

To compute the eddy viscosity, various methods are introduced, including:

- *Algebraic models* (e.g., Baldwin-Lomax): These models determine the eddy viscosity at a single point. They are limited because they were developed when powerful computational resources were not yet available.
- *One-equation transport models* (e.g., Spalart-Allmaras): These models solve a single transport equation to estimate the eddy viscosity, improving accuracy over algebraic models.
- *Two-equation transport models* (e.g., k - ω , k - ε , SST by Menter): These models solve two transport equations—one for turbulent kinetic energy (k) and another for the turbulent energy dissipation or specific dissipation (ε or ω), providing a more detailed representation of turbulence.

4.3.1 Two-equation transport models

The $k - \varepsilon$ model introduces two transport equations for k and ε which, in the standard method, are equal to [13]:

$$\frac{\partial \bar{\rho}k}{\partial t} + \frac{\partial}{\partial x_i} (\bar{\rho} \tilde{q}_i k) = \frac{\partial}{\partial x_j} \left[\left(\mu + \frac{\mu_t}{\sigma_k} \right) \frac{\partial k}{\partial x_j} \right] + G_k - \bar{\rho} \varepsilon + Y_M \quad (4.8)$$

$$\frac{\partial \bar{\rho} \varepsilon}{\partial t} + \frac{\partial}{\partial x_i} (\bar{\rho} \tilde{q}_i \varepsilon) = \frac{\partial}{\partial x_j} \left[\left(\mu + \frac{\mu_t}{\sigma_\varepsilon} \right) \frac{\partial \varepsilon}{\partial x_j} \right] + C_{1\varepsilon} \frac{\varepsilon}{k} G_k - C_{2\varepsilon} \frac{\bar{\rho} \varepsilon^2}{k} \quad (4.9)$$

In these equations, σ_k and σ_ε are empirical coefficients that govern the diffusion of the turbulent kinetic energy k and the turbulent energy dissipation ε , respectively.

In the k -equation, the term G_k represents the *production source term*, which quantifies the amount of energy extracted from the mean flow due to the gradients in the mean velocity field and transferred to the turbulence. This energy is made available at the beginning of the *inertial cascade* in the form of turbulent kinetic energy. The term $-\bar{\rho} \varepsilon$ accounts for the *destruction of turbulent kinetic energy* through viscous dissipation.

In the ε -equation, the term $C_{1\varepsilon} \frac{\varepsilon}{k} G_k$ represents the *production* of dissipation, while the term $C_{2\varepsilon} \frac{\bar{\rho} \varepsilon^2}{k}$ corresponds to its *destruction*. The constants $C_{1\varepsilon}$ and $C_{2\varepsilon}$ are also empirical and are typically calibrated based on experimental or DNS data. Finally, Y_M accounts for the *compressibility effects*, modifying the turbulence production in compressible flows.

The eddy viscosity is calculated as:

$$\mu_t = \bar{\rho} C_\mu \frac{k^2}{\varepsilon} \quad (4.10)$$

where C_μ is a constant.

The $k - \omega$ model is similar but uses $\omega = \frac{\varepsilon}{k}$, the specific dissipation rate. The equations for k and ω are as follows [13]:

$$\frac{\partial \bar{\rho}k}{\partial t} + \frac{\partial}{\partial x_i} (\bar{\rho} \tilde{q}_i k) = \frac{\partial}{\partial x_j} \left[\left(\mu + \frac{\mu_t}{\sigma_k} \right) \frac{\partial k}{\partial x_j} \right] + G_k - \beta^* \bar{\rho} \omega k \quad (4.11)$$

$$\frac{\partial \bar{\rho} \omega}{\partial t} + \frac{\partial}{\partial x_i} (\bar{\rho} \tilde{q}_i \omega) = \frac{\partial}{\partial x_j} \left[\left(\mu + \frac{\mu_t}{\sigma_\omega} \right) \frac{\partial \omega}{\partial x_j} \right] + \gamma \frac{\omega}{k} G_k - \beta \bar{\rho} \omega^2 + \bar{\rho} \sigma_d \frac{1}{\omega} \frac{\partial k}{\partial x_j} \frac{\partial \omega}{\partial x_j} \quad (4.12)$$

In the $k - \omega$ model, the transport equations for k and ω include several terms that represent different physical mechanisms. As in the $k - \varepsilon$ model, G_k denotes the *production* term, which quantifies the energy transferred from the mean flow into

turbulence due to velocity gradients. The term $-\beta^* \bar{\rho} \omega k$ represents the *destruction* of turbulent kinetic energy, where β^* is an empirical constant.

In the ω -equation, the term $\gamma \frac{\omega}{k} G_k$ is the *production* term of the specific dissipation rate, while $-\beta \bar{\rho} \omega^2$ accounts for its *destruction*. Both γ and β are empirical constants.

An additional term, $\bar{\rho} \sigma_d \frac{1}{\omega} \frac{\partial k}{\partial x_j} \frac{\partial \omega}{\partial x_j}$, appears in the equation for ω and represents a *cross-diffusion correction*, which accounts for the coupling between the gradients of k and ω . The coefficients σ_k , σ_ω , and σ_d are empirical and control the diffusion behavior of the model variables.

Overall, the main difference between the k - ε and k - ω models lies in the specific dissipation formulation and the exact form of the production/destruction terms.

Regarding their applications:

- The k - ε model is typically used for external flows, such as a flat plate.
- The k - ω model is more suitable for internal flows, for example, in turbomachinery.

The Menter SST model combines the strengths of both the k - ω and k - ε turbulence models to achieve improved accuracy in different flow regions [13].

The k - ω model performs well near walls, even in the presence of flow separation, but the results are highly sensitive to the value of ω prescribed at the inlet. This poses a problem because the boundary conditions for ω at the domain entrance are not always known with precision. In general, k is easier to determine, while ω is often found empirically, which can introduce errors into the simulation results.

On the other hand, the k - ε model is less sensitive to inlet values of ε but generally performs worse near walls, particularly in the presence of strong separations.

The Menter SST model is a hybrid approach, which behaves like k - ω near the wall and k - ε in the far field. This is achieved by rewriting the transport equation for ε in terms of ω as:

$$\omega = \frac{\varepsilon}{k} \quad \Rightarrow \quad \varepsilon = \omega k \quad (4.13)$$

As a result, the SST model has two equations for ω , which are applied depending on the flow region. To determine which equation to use, a blending function is introduced, adjusting the coefficients based on the location within the domain. This means the model switches between equations depending on whether the flow is near or far from a wall.

The eddy viscosity (μ_t) in the SST model is defined as:

$$\mu_t = \frac{\bar{\rho} a_1 k}{\max(a_1 \omega, \Omega F_2)} \quad (4.14)$$

where:

- Ω is the magnitude of the vorticity.
- F_2 is a correction function.
- a_1 is a constant.

If the dominant term in the equation is $a_1\omega$, the model behaves like $k-\omega$, whereas if ΩF_2 prevails, it behaves like $k-\varepsilon$ [13].

4.3.2 One-equation transport model

The Spalart-Allmaras (SA) model is a one-equation turbulence model specifically developed for high Reynolds number flow simulations [13]. Unlike two-equation models such as $k-\varepsilon$ and $k-\omega$, the SA model directly introduces a transport equation for a modified eddy viscosity $\tilde{\nu}$, which is then used to compute the effective eddy viscosity μ_t .

The transportation equation is computed as:

$$\frac{d\rho\tilde{\nu}}{dt} + \frac{d\rho q_i\tilde{\nu}}{dx_i} = \rho(P - D) + \frac{1}{\sigma} \frac{d}{dx_i} \left[\rho(\nu + \tilde{\nu}) \frac{d\tilde{\nu}}{dx_i} \right] + \frac{Cb_2}{\sigma} \rho \frac{d\tilde{\nu}}{dx_i} \frac{d\tilde{\nu}}{dx_i} - \frac{1}{\sigma} (\nu + \tilde{\nu}) \frac{d\rho}{dx_i} \frac{d\tilde{\nu}}{dx_i} \quad (4.15)$$

This equation includes the following main terms:

- Production P :

$$P = C_{b1} \tilde{S} \tilde{\nu}$$

It depends on the magnitude of the modified strain rate tensor \tilde{S} , this term is modified to stabilise the model. If $S \geq 0$, turbulent viscosity is generated. The production term is proportional to $\tilde{\nu}$, so if the field is initially laminar with $\tilde{\nu} = 0$, there is no possibility of a transition to turbulence. This is because the production term is proportional to $\tilde{\nu}$, but if $\tilde{\nu}$ is not there the term will never be created. So the flow is considered turbulent from the beginning, as the Reynolds number is high.

- Destruction D :

$$D = C_{\omega 1} f_w \left(\frac{\tilde{n}u}{d} \right)^2$$

d represents the distance from the wall, meaning that as one approaches the wall, dissipation tends to infinity.

- Diffusion: a term that accounts for the diffusion of turbulent viscosity transport through the divergence of the flow.

- Cross-production: it corrects the equation to ensure stability and influences diffusion.

The SA model requires specific boundary conditions to ensure the correct development of turbulence:

- *Solid walls:*

$$\tilde{\nu} = 0$$

This is a homogeneous Dirichlet condition, ensuring that the turbulent viscosity is zero at the wall.

- *Inlet:*

$$\frac{\tilde{\nu}}{\nu} \geq 3$$

This sets a minimum value to guarantee a fully turbulent flow. If the initial value of $\tilde{\nu}$ is too low, the flow will never transition to turbulence, as production depends directly on $\tilde{\nu}$. This condition is a recommendation from the authors of the method to prevent underestimation of inlet turbulence.

Spalart-Allmaras is the most stable method, while the others can present stiffer initial problems and therefore need a very low time step at the beginning (CFL condition) [13]. This is why it is also the most widely used in industry.

4.3.3 CFL Condition

The CFL condition is linked to the CFL number. It is a fundamental dimensionless number in the numerical solution of partial derivative equations, particularly for finite difference and finite volume methods [26]. It defines a stability criterion for explicit numerical integration methods.

It is defined as:

$$CFL = \frac{\lambda \Delta t}{\Delta x} \tag{4.16}$$

where:

- λ is the characteristic velocity of the flow (e.g., the wave propagation speed)
- Δt is the time step of the simulation
- Δx is the spatial discretization step

For two-dimensional or three-dimensional problems, the CFL number can be generalized by considering the sum of velocity contributions along different directions:

$$CFL = \sum_i \frac{\lambda_i \Delta t}{\Delta x_i} \quad (4.17)$$

For hyperbolic equations:

$$CFL = \max \left(\frac{\lambda_i \Delta t}{\Delta x_i} \right) \quad (4.18)$$

where λ_i represents the eigenvalues of the hyperbolic system.

The CFL condition says that the physical dependency domain must be included in the numerical dependency domain. In fact, it has a clear physical interpretation: it represents the ratio between the distance travelled by physical information in a time interval Δt and the spatial resolution of the numerical grid Δx . If the CFL number is too large, the information may "jump" multiple grid cells in a single time step, leading to unstable or non-physical solutions [26].

This is a very important consideration especially when simulating turbulence to ensure the stability of the method, often the use of an adaptive CFL number becomes of interest: the time step is dynamically adjusted to maintain a constant CFL number throughout the simulation. This helps to ensure stability and accuracy, especially in simulations with significant speed variations.

4.4 Convective Fluxes

Considering the Euler equations or the convective part of the NS, there are several numerical methods to calculate the convective fluxes at the edge of the cell, which are divided into upwind and centred schemes [13].

In particular, upwind methods are divided into flux difference splitting methods, such as Godunov, Osher-Enquist-Pandolfi and Roe, and flux vector splitting methods, including the classical FVS and AUSM.

Unlike upwind methods, centred schemes do not explicitly account for the hyperbolic nature of the equations, meaning they do not directly consider wave propagation. Instead, they compute the fluxes by averaging the contributions from the left and right of the cell without explicitly considering wave propagation.

However, a purely centred scheme is unstable, so an explicit numerical viscosity is added to ensure stability. Examples of such methods include Lax-Friedrichs and Jameson-Schmidt-Turkel (JST) [13].

4.4.1 Roe method

The most widely used convective scheme in density-based solvers is the flux-difference splitting scheme developed by Roe (1981). This first-order method belongs to Godunov-type schemes and is based on solving a Riemann problem. A key feature of this approach is that the flux at the control volume face is interpolated using both upstream and downstream values, and the final flux is obtained as the average of these interpolations. Furthermore, the amount of numerical dissipation is controlled by a matrix of eigenvalues, which depends on the difference between the velocity of the fluid and the speed of sound [25].

The MUSCL scheme (Monotone Upstream-Centred Schemes for Conservation Laws) extends the Roe scheme to higher orders, as proposed by Van Leer (1979). This is accomplished by applying higher-order interpolations both upstream and downstream of the control volume face, improving accuracy while maintaining numerical stability [25].

4.4.2 JST method

The JST method is a centred scheme widely used in computational fluid dynamics for structured and unstructured grids.

A key characteristic of the JST scheme is its large stencil: when computing fluxes at a given cell j , it requires information from neighbouring cells $j + 1$, $j + 2$, $j - 1$ and $j - 2$. This large stencil improves accuracy but increases computational complexity [13].

JST computes the numerical flux at the face between cells as:

$$F_{j+\frac{1}{2}} = \frac{F_j + F_{j+1}}{2} - D_{j+\frac{1}{2}} \quad (4.19)$$

This formulation follows the standard centred approach, where the flux at an interface is obtained by averaging the fluxes from the left and right neighbouring cells. However, a purely centred scheme is unstable, so JST introduces a dissipative term $D_{j+\frac{1}{2}}$ to enhance numerical stability.

The JST scheme introduces artificial viscosity through a dissipation term that combines second-order and fourth-order dissipation:

$$D_{j+\frac{1}{2}} = \epsilon_{j+\frac{1}{2}}^2 \Delta U_{j+\frac{1}{2}} - \epsilon_{j+\frac{1}{2}}^4 (\Delta U_{j+\frac{3}{2}} - 2\Delta U_{j+\frac{1}{2}} + \Delta U_{j-\frac{1}{2}}) \quad (4.20)$$

The dissipation term consists of two components. The second-order dissipation term ϵ^2 acts as a shock-capturing term, ensuring numerical stability and is typically associated with Lax-Friedrichs type dissipation. The fourth-order dissipation term ϵ^4 helps preserve accuracy in smooth regions by damping high-frequency oscillations.

The balance between these two dissipation terms ensures both stability and accuracy in the numerical solution.

To control the level of dissipation, JST introduces a pressure-based sensor:

$$S_{j+\frac{1}{2}} = \max(S_j, S_{j+1}) \quad (4.21)$$

where:

$$S_j = \frac{|P_{j+1} - 2P_j + P_{j-1}|}{|P_{j+1} + 2P_j + P_{j-1}|} \quad (4.22)$$

This pressure sensor detects shock waves and high-gradient regions, ensuring that dissipation is applied where needed, without affecting smooth regions unnecessarily. If the pressure gradient is high (e.g., near a shock), S_j increases, activating stronger dissipation. Conversely, if the pressure gradient is low (smooth regions), S_j remains small, minimizing artificial dissipation.

The dissipation coefficients are defined as:

$$\epsilon_{j+\frac{1}{2}}^2 = K_2 S_{j+\frac{1}{2}} \lambda_{\max, j+\frac{1}{2}} \quad (4.23)$$

$$\epsilon_{j+\frac{1}{2}}^4 = \max\left(0, K_4 \lambda_{\max, j+\frac{1}{2}} - C_4 \epsilon_{j+\frac{1}{2}}^2\right) \quad (4.24)$$

where $K_2 = 1$, $K_4 = \frac{1}{32}$, and $C_4 = 2$. The fourth-order dissipation ϵ^4 is indirectly controlled by ϵ^2 , which in turn is influenced by the pressure sensor [13].

4.5 Boundary layer resolution requirements

For evaluating the resolution of the first layer of mesh cells near the wall and selecting the appropriate wall treatment approach it is essential to select a proper value of y^+ [27]. This parameter is a dimensionless quantity used in turbulence modelling to characterise the distance from the wall in turbulent flows.

It is defined as:

$$y^+ = \frac{y u_\tau}{\nu} \quad (4.25)$$

where:

- y = normal distance from the wall to the first computational grid point,
- u_τ = friction velocity ($u_\tau = \sqrt{\tau_w/\rho}$, with τ_w being the wall shear stress),
- ν = kinematic viscosity of the fluid.

The y^+ value indicates which region of the turbulent boundary layer the first grid point lies in:

1. $y^+ < 5$: *Viscous sublayer*. Viscosity dominates, and the velocity profile is nearly linear. Requires a very fine mesh to resolve this layer in CFD.
2. $5 < y^+ < 30$: *Buffer layer*. Both viscosity and turbulence contribute. This region is difficult to model accurately.
3. $y^+ > 30$: *Log-law region*. Flow is dominated by turbulence, and velocity follows the log-law:

$$\frac{U}{u_\tau} = \frac{1}{\kappa} \ln(y^+) + B \quad (4.26)$$

where $\kappa \approx 0.41$ is the von Kármán constant and $B \approx 5.0$ is an empirical constant.

Depending on the chosen approach, the y^+ value determines the wall treatment strategy[27]:

1. Low y^+ ($y^+ < 1$) → Wall-Resolved Approach
 - The mesh must resolve the viscous sublayer.
 - Used with models like k- ω SST, SA and LES.
 - High computational cost.
 - Application in aerospace propulsion.
2. High y^+ ($y^+ > 30$) → Wall-Modelled Approach
 - The first grid point is in the log-law region.
 - Uses wall functions to avoid excessive grid refinement.
 - Applied to models like k- ϵ or k- ω SST with wall functions.
3. Intermediate y^+ values ($5 < y^+ < 30$)
 - Avoided in CFD because wall functions may not work well, and the mesh may not be fine enough to resolve the viscous sublayer.

4.6 Stator-Rotor Interaction Methods

The interaction between the stator and rotor rows in a supersonic turbine is a highly complex phenomenon, characterised by unsteady and turbulent effects that significantly affect the aerodynamic and thermodynamic performance of the system.

As the flow passes through the stator row, it generates turbulent wakes and shock waves, which are then intercepted by the moving rotor. This behaviour introduces unsteady variability into the flow field, complicating the prediction and optimisation of performance.

One of the main problems in the interaction between stator and rotor rows is related to the presence of turbulent wakes that form downstream of the stator, impact on the rotor blades and affect the ability of the boundary layer to remain attached to the wall, thus altering its performances and reducing its efficiency. If the rotor passes through these wakes intermittently, the flow becomes inherently unsteady, complicating the analytical and numerical modelling of the phenomenon [13]. In addition, a fundamental role is played by shock waves and expansion fans generated in inter-row zones. Reflected shock waves can interact with the rotor blades, creating pressure discontinuities and altering the velocity profile.

Dealing with these phenomena requires careful numerical analysis, often supported by mediation techniques such as mixing plane or advanced CFD models that take into account turbulence and unsteady effects.

4.6.1 Mixing Plane

To reduce computational cost, the initial approaches implemented are generally steady-state. One of the most commonly used methods is the so-called mixing plane method, which consists of introducing an averaging plane located approximately halfway between the trailing edge of the stator and the leading edge of the rotor [25]. An example of computational results obtained using this technique is shown in figure 4.2, derived from an analysis performed with SU2 as in reference [28].

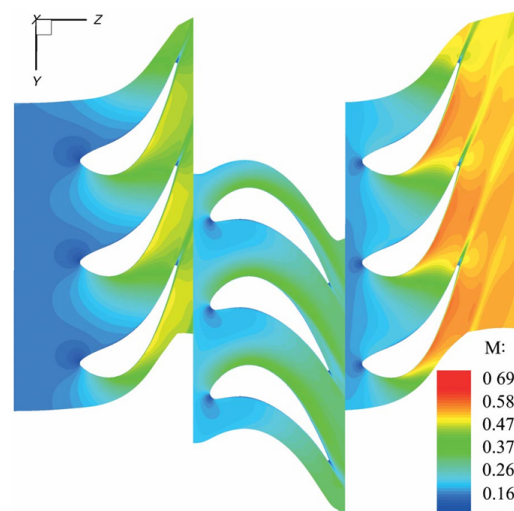


Figure 4.2: SU2 analysis example with Mixing Plane [28]

With this method, the flow is averaged in the circumferential direction, eliminating temporal variations and consequently neglecting the unsteady interaction between the two blade rows. As a result, the stator and rotor solutions tend to converge towards a steady-state solution.

The averaging process in the mixing plane approach is conceptually equivalent to an instantaneous mixing of the non-uniform flow at a specific location, rather than a gradual mixing occurring throughout the downstream blade row. The fundamental assumption behind this method is that the mixing losses introduced at the mixing plane are equivalent to those that would naturally occur as the real flow mixes within the downstream row [24].

However, as Denton cautioned, this assumption lacks a rigorous theoretical foundation:

"There is no a priori theory to justify this assumption" [29].

A comparison between this method and unsteady simulations is presented in [24], where the entropy distributions show the presence of an entropy jump at the mixing plane. This phenomenon is intrinsic to the mixing plane approach, as it results from the circumferential averaging process, which in turn reduces the discrepancies in the overall losses between the steady-state and unsteady modelling techniques.

In steady-state calculations, the mixing of flow non-uniformities occurs instantaneously at the mixing plane, rather than progressively within the rotor passage. Consequently, in the region downstream of the mixing plane, the rotor is subject to a lower entropy change than in the unsteady case. However, when considering the cumulative entropy generation from the mixing plane and the rotor, the final entropy level remains generally comparable to that obtained in an unsteady simulation.

Furthermore, the intensity of the entropy discontinuity at the mixing plane is directly influenced by the non-uniformity of the flow in the pitch direction, with a more pronounced effect observed under transonic operating conditions.

4.6.2 Harmonic Balance

The harmonic balance method is a mathematical approach that allows one to solve unsteady effects at discrete sets of frequencies in the frequency domain instead of the time domain. It is particularly useful in computational fluid dynamics to study periodic or quasi-periodic phenomena with a more efficient representation than conventional methods [30].

The significant increase in computational resources has led to an incentive to extend single-passage and steady-state methods for unsteady simulations, rather than directly adopting direct solutions in the design environment. This basic consideration constitutes the general motivation for the development of the Fourier

modelling approach. The basic requirement is the existence of periodicity, which is a fundamental characteristic of flows in turbomachinery. These frequency domain approaches follow the same Fourier modelling principle and share a common basic characteristic: a non-linear harmonic solution N_f is equivalent to $2N_f + 1$ steady flow solutions. A key feature of frequency domain approaches is that a problem involving the solution of a set of steady-state flow equations is effectively transformed into the solving of a set of time-independent steady flow equations [31].

A signal can be approximated as a truncated Fourier series and when applied to the solution vector, it takes the form shown in equation 4.27

$$U = \bar{U} + \sum_{n=1}^N A_n \sin(n\omega t) + B_n \cos(n\omega t) \quad (4.27)$$

The Blade Passing Frequency (BPF) dominates the flow spectrum, so a single frequency is often considered, reducing the series to the form given in equation 4.28.

$$U = \bar{U} + A \sin(\omega t) + B \cos(\omega t) \quad (4.28)$$

Additionally, the Hall's harmonic balance approach [31] proposes to solve the non-linear harmonic flow equations considering the Unsteady Reynolds-Averaged Navier-Stokes (URANS) equations (Eq. 4.29).

$$\frac{\partial U}{\partial t} + R(U) = 0 \quad (4.29)$$

$$\omega A \cos(\omega t) - \omega B \sin(\omega t) = -R(\bar{U} + A \sin(\omega t) + B \cos(\omega t)) \quad (4.30)$$

To solve equation 4.30 for the three unknowns (A, B, \bar{U}), three equations are required, evaluated at three different time instances.

$$\omega A \cos(\omega t_0) - \omega B \sin(\omega t_0) = -R(\bar{U} + A \sin(\omega t_0) + B \cos(\omega t_0)) \quad (4.31)$$

$$\omega A \cos(\omega t_1) - \omega B \sin(\omega t_1) = -R(\bar{U} + A \sin(\omega t_1) + B \cos(\omega t_1)) \quad (4.32)$$

$$\omega A \cos(\omega t_2) - \omega B \sin(\omega t_2) = -R(\bar{U} + A \sin(\omega t_2) + B \cos(\omega t_2)) \quad (4.33)$$

In general, $2N + 1$ time instances are required to solve for the unsteady solution U , which is characterized by a single frequency (N being the number of frequencies).

This approach has some drawbacks. It is less accurate than URANS, less stable and requires more time to achieve residual convergence. However, it has significant advantages and one of its main benefits is the lower computational cost compared to accurate simulations in time, although this depends on the number of frequencies [31].

One important assumption of the harmonic balance method is the periodicity of the unsteady signal. While this is a reasonable approximation in many turbomachinery applications, such as rotor-stator interactions, blade clocking studies and tonal noise analysis, it limits the method's capability to capture broadband or transient phenomena. As a result, purely stochastic or strongly aperiodic flow features, such as vortex shedding with variable shedding rates or transient shock motions, may not be accurately resolved.

Despite these limitations, the harmonic balance method provides an efficient alternative to time-domain simulations when the dominant frequencies of the unsteady phenomena are known a priori. Recent developments have also extended the framework to support multiple frequencies (multi-harmonic approaches), making it applicable to more complex blade row interactions and non-synchronous configurations.

In turbomachinery design environments, where computational efficiency is essential, the harmonic balance method represents a valuable compromise between time-accurate simulations and steady-state approximations. When combined with advanced turbulence models its predictive capability can be significantly enhanced while maintaining manageable computational cost.

Chapter 5

Computational Fluid Dynamics Simulations

5.1 Mesh Generation

The geometry of a single blade is generated using UMG2, an in-house meshing software for unstructured meshes. The computational domain is discretized with triangular elements and wall-clustered quadrilateral elements near the wall to ensure a $y^+ < 1$. To achieve an appropriate boundary layer resolution, the following relation is applied:

$$\Delta y = L \cdot y^+ \cdot \sqrt{80} \cdot Re_x^{1/14} \cdot \frac{1}{Re_L} \quad (5.1)$$

This equation is derived from the reference [32] and has been demonstrated to be highly effective.

Furthermore, different cell dimensions are used as input to generate various types of meshes: coarse, medium, fine and ultrafine.

An example of stator mesh is shown in the figure 5.1.

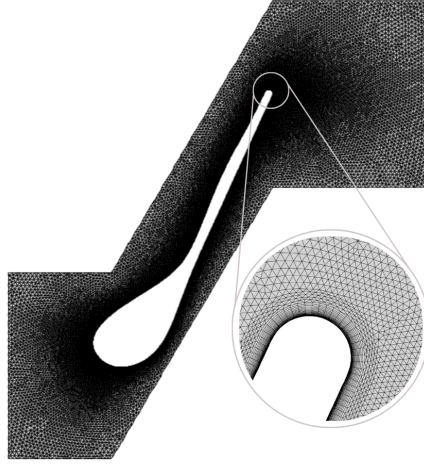


Figure 5.1: First stator coarse mesh

5.2 Mesh Sensitivity

To select the optimal mesh and reduce grid-discretization errors, a mesh sensitivity analysis is performed for the second stator, specifically for the stator of the turbine stage with the medium expansion ratio.

In particular, the analysis starts with the coarse mesh, where the average cell size h is approximately $1/50$ of the stator pitch. Once the simulation is run with this mesh, the total area of the computational domain is considered, ensuring consistency in the refinement process. To systematically improve resolution, a refinement factor of $r = 1.33$ is applied, allowing the determination of the required cell size for the next finer mesh using the relation $h_{required} = h_{actual}/r$. After generating and running the second, finer mesh, the actual number of cells is known, allowing the calculation of the corresponding actual cell size h_{actual} . At this stage, it is verified that this value remains consistent with the requirement of $r > 1.33$, as explained in reference [33]. This iterative process is then repeated, with the new required cell size continuously updated and refined using the same formula. The procedure continues until the ultrafine mesh is reached, ensuring a systematic reduction of discretization errors and progressively improving numerical accuracy.

After generating the meshes, the next step is to verify the entropy generation for each mesh and evaluate its deviation from the finest mesh. Its value is expressed as in equation 5.2, where s_{out} and s_{in} are the outlet and inlet entropy values, averaged over the respective boundaries using the mixed-out procedure [34].

$$s_{gen} = \frac{s_{out} - s_{in}}{s_{in}} \quad (5.2)$$

The results are illustrated in the figure 5.2.

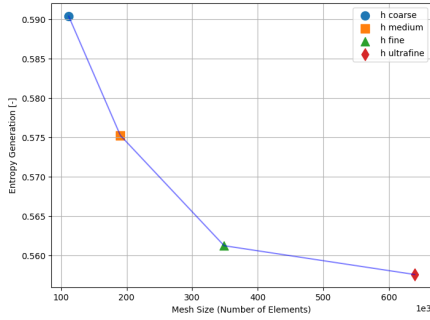


Figure 5.2: Entropy Generation

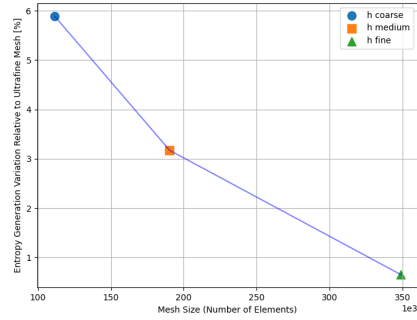


Figure 5.3: Entropy Generation Variation

To reduce computational cost, the ultrafine mesh is avoided in favour of one of the other meshes, provided that the variation in Entropy Generation does not exceed 2% compared to the ultrafine mesh. The variations among the different meshes are illustrated in figure 5.3.

The mesh with an Entropy Generation variation below 2% compared to the ultrafine mesh is the fine mesh. Therefore, the same h is used for all other stator and rotor geometries.

5.3 Isolated Stators Analysis

After generating the meshes for the stators of the three turbine stages, the next step is to set up the simulations for the isolated stators. The SU2 software is utilized, leveraging the computational resources of the DelftBlue cluster [35] to run the simulations efficiently.

The main parameters are illustrated in table 5.1.

The simulations implement a RANS solver that models turbulence according to the SA method. Additionally, the "Ideal gas" model is used to simulate air, defined by the specific heat ratio γ and the gas constant R . A constant viscosity value is assumed, calculated along an isentropic expansion using the same expansion ratio, as well as a constant thermal conductivity which employs a constant Prandtl number approach.

Table 5.1: Main simulation parameters of the axial stators

Parameter	First Stator	Second Stator	Third Stator	Unit
Free-stream Mach number	0.34	0.41	0.44	-
Reduced Temperature T_r	7.55	7.55	7.55	-
Reduced Pressure P_r	2.11	2.11	2.11	-
Free-stream Density	25.64	24.93	24.64	kg/m^3
Heat capacity ratio γ	1.342	1.375	1.343	-
Turbulent viscosity ratio	100	100	100	-
Dynamic viscosity	3.38×10^{-5}	3.14×10^{-5}	2.93×10^{-5}	$kg/(m \cdot s)$
Outlet Static Pressure	2564676.89	1246602.92	877790.90	Pa

The non-reflecting boundary conditions by Giles are considered. The objective of formulating non-reflecting boundary conditions is to prevent spurious, non-physical reflections at inflow and outflow boundaries, ensuring that the computed flow field remains independent of the far-field boundary locations. This enhances accuracy and computational efficiency, allowing for a smaller computational domain [21].

Meanwhile, the mixed-out approach is implemented for the averaging process. Unlike simple mass-averaging or area-averaging methods, which primarily weight properties based on flow distribution, the mixed-out approach accounts for entropy variations and non-uniformities in the flow. It computes an equivalent uniform flow state where mass, momentum and total enthalpy are preserved while eliminating local distortions caused by wakes, shocks, and boundary layers. This results in a more physically meaningful representation of the flow, particularly in turbomachinery applications where strong variations in thermodynamic properties occur due to compressibility effects [36].

Two simulations are performed for each stator:

1. A first-order simulation using the Roe solver, which serves as an initialization step. This helps the solution to converge more efficiently before proceeding to higher-order accuracy.
2. A second-order simulation using the JST solver, providing improved accuracy.

The time discretization is based on the implicit Euler method, while the turbulent convective method follows a scalar upwind approach.

An adaptive CFL number is considered, while FGMRES is used as the linear solver, with LU-SGS as the preconditioner.

FGMRES is an iterative linear solver used to solve large, sparse systems of linear equations, which arise when solving discretized governing equations (e.g., Navier-Stokes equations). It is an extension of the GMRES (Generalized Minimal Residual) method, but it allows for a flexible choice of preconditioners at each

iteration. LU-SGS is a preconditioning technique that speeds up the convergence of iterative solvers like FGMRES. It is based on the Gauss-Seidel method but applied in a lower-upper factorized form to approximate the inverse of the system matrix [13].

Furthermore, efficiency is set as the objective function.

5.3.1 First Stator Results

Mach number and pressure distributions of the first stator are illustrated in figures 5.4 and 5.5.

As expected, a wake forms at the trailing edge, which influences the evolution of the flow. To adapt to the conditions of the wake, the flow expands within the diverging section of the nozzle and through expansion fans in the post-expansion phase, eventually leading to the formation of two distinct shock waves, clearly visible in the pressure contour. The right-running shock propagates towards the rotor, while the left-running wave impinges on the adjacent vane, generating a reflection.

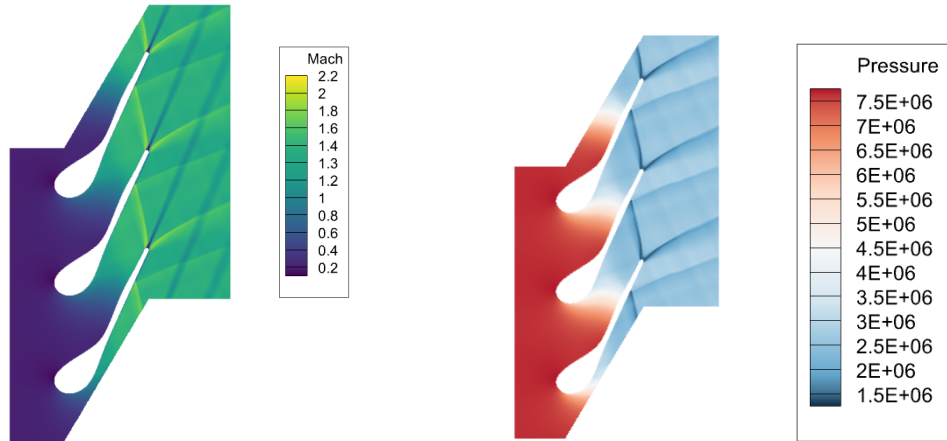


Figure 5.4: Mach number distribution of the first stator **Figure 5.5:** Pressure distribution of the first stator

The flow becomes sonic exactly at the throat, demonstrating an effective initial design. This is highlighted in the figure 5.6 through the contour lines, where the red line represents the sonic line.

As shown, the sonic line assumes a curved shape across the throat region. This curvature is a well-known feature in supersonic nozzle or turbine throat designs, where the sonic line bends in response to the local pressure and velocity gradients. Specifically, it tends to follow the streamline curvature and adapts to the pressure

field generated by upstream and downstream geometrical features, including blade loading and shock-wave interactions.

The presence of a smooth and continuous sonic line indicates that the acceleration to Mach 1 is gradual and primarily one-dimensional near the throat, which is desirable for minimizing losses. However, deviations from a straight line, such as the curvature observed in the figure, occur due to span-wise or cross-channel pressure variations and shock-induced perturbations.

This behaviour is consistent with classical analyses of transonic throat flows in turbomachinery, as discussed for example in [12] and [37], where the sonic line is shown to deviate from a straight profile when subject to non-uniformities in the flow field or blade passage geometry.

In contrast, in idealized geometries such as convergent nozzles with parallel walls, the flow tends to remain nearly one-dimensional in the throat, and the sonic line appears as a straight segment perpendicular to the main flow direction. This is due to the absence of transverse pressure gradients and span-wise variations.

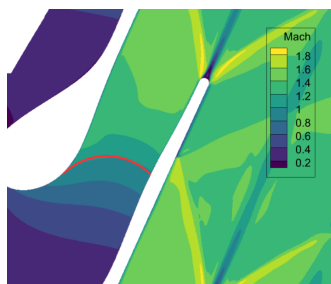


Figure 5.6: Sonic Line



Figure 5.7: Shock-Boundary layer interaction

As the shock wave impinges on the vane, there is a thickening of the boundary layer, visible in the figure 5.7. This occurs because the reduction of the kinetic energy of the fluid and the adverse pressure gradient near the wall cause the boundary layer to separate. As shown in the figure 5.8, the separation generates a recirculation region; however, further downstream, the flow accelerates again, allowing the boundary layer to reattach to the blade surface, as in figure 5.9.

The image 5.10 illustrates the flow behaviour in the trailing edge region, highlighting the presence of the wake and of a recirculation region. In the zoomed-in section, it can be observed that the flow decelerates, leading to boundary layer separation. This phenomenon results from the adverse pressure gradient, whose effect is visible in the velocity profiles: a progressive velocity reduction is observed up to the separation point, followed by the characteristic behaviour of a separated flow.

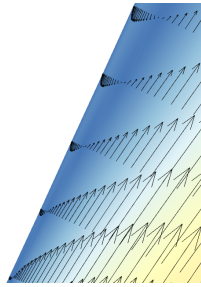


Figure 5.8: BL separation

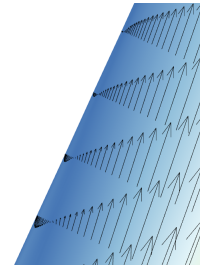


Figure 5.9: BL reattachment

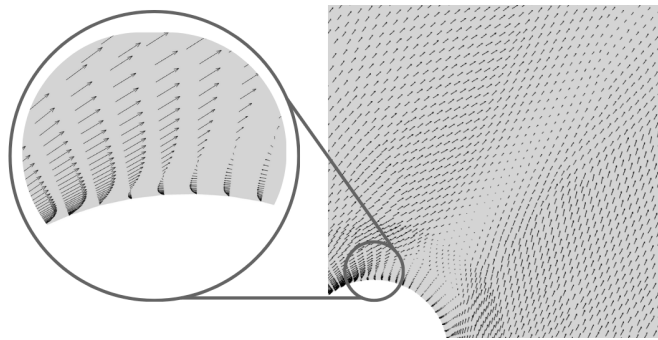


Figure 5.10: Wake and Boundary Layer

The residuals are presented in the graph 5.11, where it can be observed that the conservative variables decrease by eight orders of magnitude. Since the y-axis is in logarithmic scale, this indicates the convergence of the results.

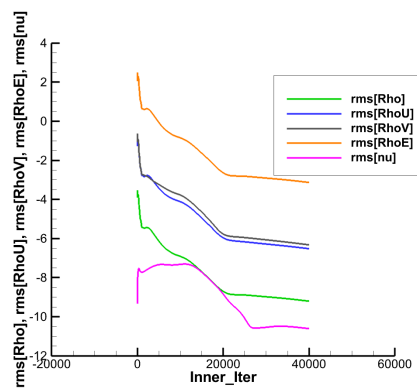


Figure 5.11: Residuals of isolated first stator

5.3.2 Second Stator Results

The results for the isolated stator of the turbine stage with a medium expansion ratio are shown in figures 5.12 and 5.13. In this case, a particular phenomenon occurs: the left-running shock wave does not impact the adjacent blade due to a significant post-expansion. This discrepancy could be attributed to a potential error in the divergent section of the nozzle, where a strong post-expansion might have been considered, or it could result from an inaccurate downstream pressure value in the TurboSim output.

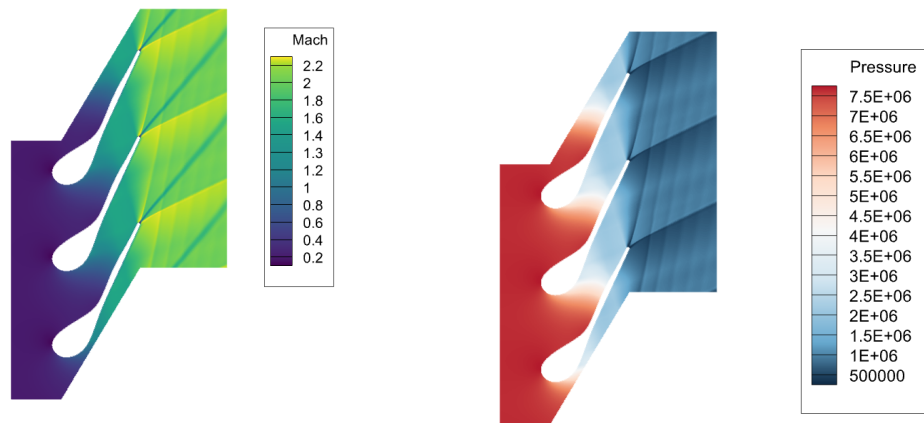


Figure 5.12: Mach number distribution of the second stator **Figure 5.13:** Pressure distribution of the second stator

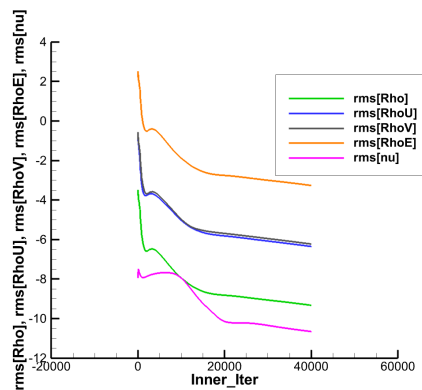


Figure 5.14: Residuals of isolated second stator

The other considerations regarding the sonic line and the wake remain the same

as in the previous case.

Similarly, in this case, the residuals decrease by eight orders of magnitude, as shown in figure 5.14.

5.3.3 Third Stator Results

The results for the isolated stator of the turbine stage with a high expansion ratio are shown in figures 5.15 and 5.16.

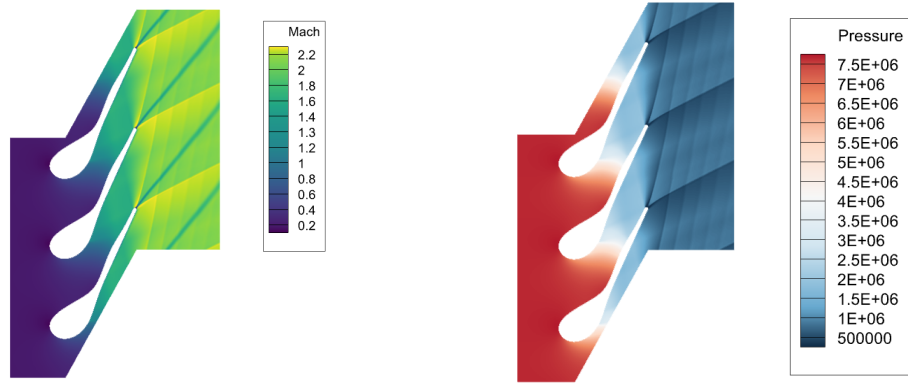


Figure 5.15: Mach number distribution of the third stator **Figure 5.16:** Pressure distribution of the third stator

The other considerations remain the same as in the previous cases.

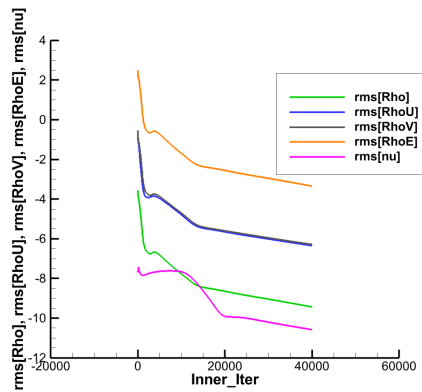


Figure 5.17: Residuals of isolated third stator

Furthermore, it is possible to observe a thickening of the shocks downstream in the figure 5.16 compared to the other cases, indicating a greater expansion and

stronger shocks, which result in a lower downstream pressure.

Similarly, in this case, the residuals decrease by eight orders of magnitude, as shown in figure 5.17.

5.4 Stator-Rotor Analysis

For the analysis of the entire turbine stage, the same computational setup and boundary conditions described in the previous section are applied, taking into account the rotor downstream pressure.

First, steady-state analyses are performed using the mixing plane method with linear interpolation, followed by unsteady analyses conducted with the harmonic balance approach.

5.4.1 Mixing Plane Method Results

Figures 5.18 and 5.19 present the results for the second turbine stage.

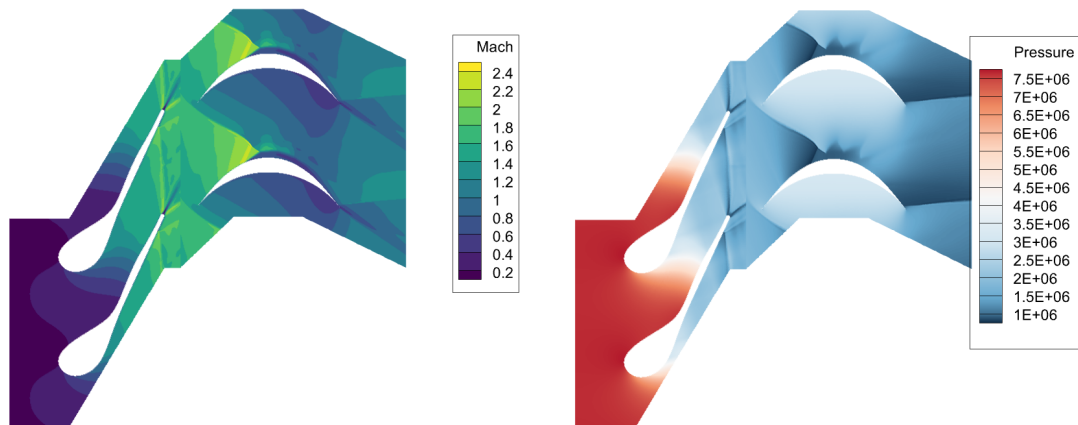


Figure 5.18: Absolute Mach number distribution of the second stage

Figure 5.19: Pressure distribution of the second stage

The left-running shock wave at the stator trailing edge impacts on the adjacent vane and is reflected, a phenomenon not observed in the isolated stator results.

The pressure at the stator outlet is higher than the value predicted by TurboSim:

- P_1 (stator): 1246602.92 Pa
- P_1 (stator-rotor): 1706618.0 Pa

There are two possible explanations for this discrepancy.

The first possibility is that the design of the divergent section of the stator is not optimal, as previously discussed.

The second possibility is that the rotor is relatively large and causes substantial blockage. This blockage would increase the upstream pressure at the stator outlet, effectively reducing the amount of post-expansion observed during unsteady operation.

A possible improvement could be to perform isolated stator analysis using the output pressure of the coupled stator-rotor analysis to better capture interaction effects.

The most interesting result for the purposes of this project is the relative Mach number and its distribution is shown in the figure 5.20.

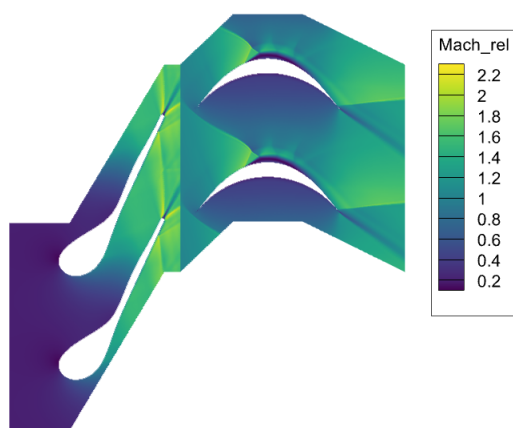


Figure 5.20: Relative Mach Distribution of the second stage



Figure 5.21: Zoomed-in view

A bow shock is formed upstream of the leading edge of the rotor. This shock wave impinges on the suction side of the adjacent blade, causing the boundary layer to separate.

The characteristics and position of the bow shock are also strongly influenced by the rotor leading edge geometry. In this case, the leading edge is sharp, which contributes to the formation of a stronger and more defined shock upstream of the rotor blade. A sharper geometry typically promotes earlier shock formation and can increase flow sensitivity to incidence variations. However, this configuration represents a conservative approach: the sharper the edge, the more challenging the flow interaction, particularly regarding shock–boundary layer interaction and potential separation. This allows the analysis to capture worst-case aerodynamic phenomena and ensure robustness in the design, as a sharper leading edge promotes the formation of a bow shock farther upstream compared to a rounded profile. This is because the abrupt geometry gives the incoming supersonic flow less opportunity

to gradually adjust its direction. As a result, a stronger and more forward-positioned shock is needed to deflect the flow appropriately. In contrast, a rounded leading edge allows for partial expansion and smoother turning, which tends to delay the formation of the shock and reduce its intensity.

Nevertheless, such sharp profiles at both leading and trailing edges, while useful in the early design phase, are not realistic for final manufacturing. In practice, the blades will require a more rounded leading edge for structural integrity and improved thermal resistance.

The average rotor inlet relative Mach number, represented by the red dot in figure 5.21, is equal to 1.112, while the Mach number after the bow shock is 0.823. The mean line design indicates that the Mach target is $M_{rel, rotor inlet} = 1.11$, which is consistent with the CFD analysis.

Regarding the third turbine stage, the results are shown in figures 5.22 and 5.23.

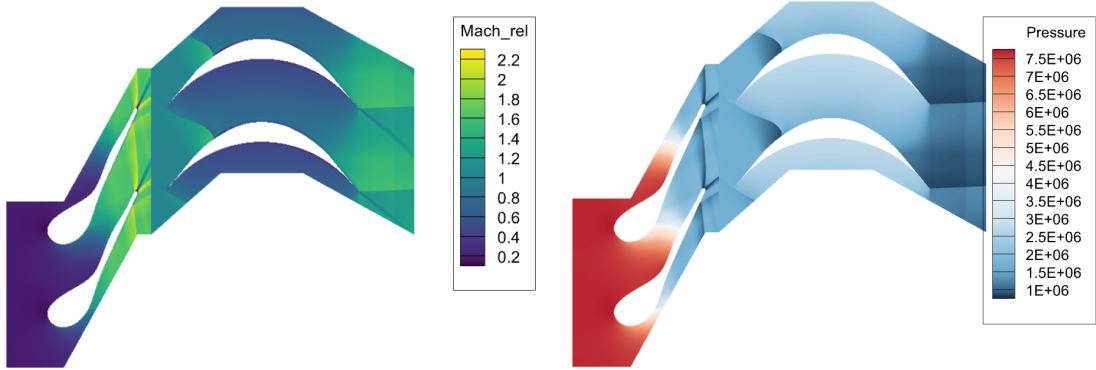


Figure 5.22: Relative Mach number distribution of the third stage

Figure 5.23: Pressure Distribution of the third stage

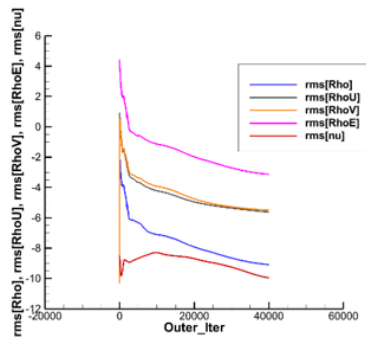


Figure 5.24: Residuals steady stator-rotor analysis.

In this case, the rotor inlet relative Mach number is lower than the value predicted

by TurboSim. A possible reason could be the adjustment of the rotor pitch to match the stator value. This modification is performed to ensure compatibility for running unsteady simulations, but it may have caused a variation in flow conditions.

In figure 5.24, an example of residual convergence is also shown for the steady stator-rotor analysis.

5.4.2 Harmonic Balance Method Results

To compute harmonic balance simulations, only the BPF is considered. Consequently, the results are obtained for three time instances, corresponding to $2N + 1$ solutions.

The main quantities implemented to run the simulations are expressed in the equation 5.3, while the results for the second stage are presented in table 5.2.

$$BPF = \frac{1}{T}, \quad T = \frac{Pitch}{u} \quad \Rightarrow \quad \omega = 2\pi BPF \quad (5.3)$$

Parameter	Value
u	338.34 m/s
Pitch	0.0215 m
T	0.0000635455 s
BPF	15736.75555 Hz
ω	98876.95 rad/s

Table 5.2: Second turbine HB parameters

These analyses are conducted only for the second turbine stage and the following figures show the results for each time instance.

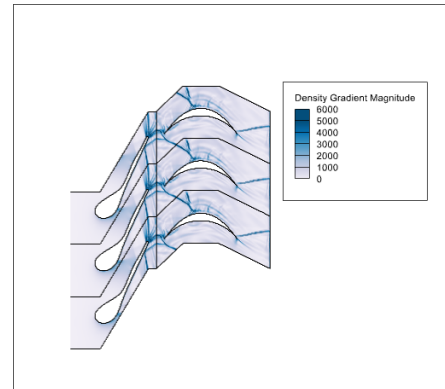
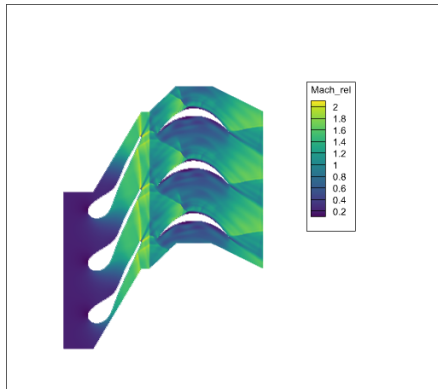


Figure 5.25: Relative Mach number distribution of the first time instance **Figure 5.26:** Density gradient of the first time instance

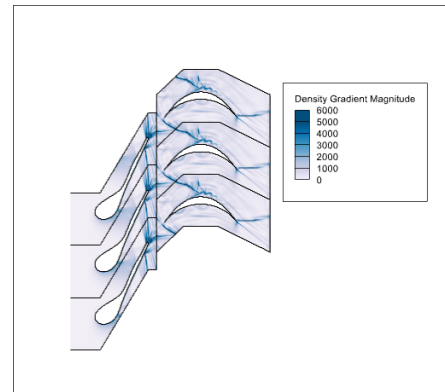
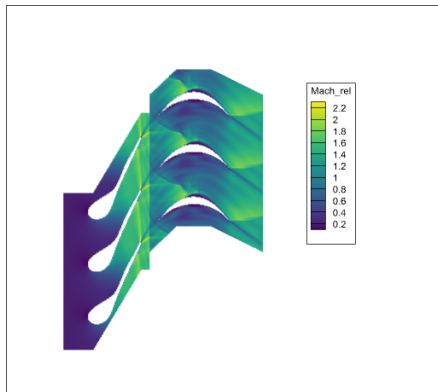


Figure 5.27: Relative Mach number distribution of the second time instance **Figure 5.28:** Density gradient of the second time instance

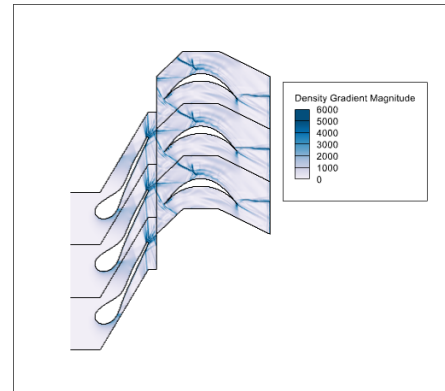
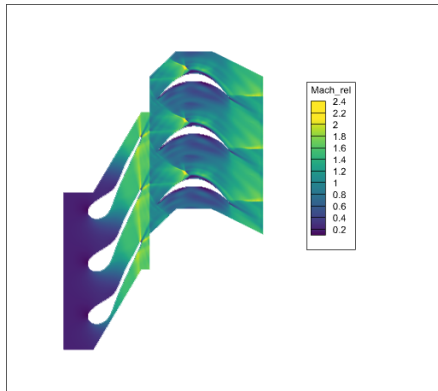


Figure 5.29: Relative Mach number distribution of the third time instance **Figure 5.30:** Density gradient of the third time instance

As the rotor moves, the interaction between the stator and rotor, in particular between the bow shock and the shock waves exiting the stator, varies. Consequently, the rotor inlet relative Mach number changes at different time instants, reaching values of 1.11 at the first instant, 1.09 at the second and 1.02 at the third. Understanding the unsteady nature of the problem and, consequently, the significance of these analyses becomes crucial.

An effective approach to verifying the unsteadiness of the flow is to analyse the blade loading by examining the pressure distribution along the stator and rotor blades, with particular emphasis on the rotor. Variations in the pressure profiles over time provide insight into the transient aerodynamic forces acting on the blades and allow for the assessment of unsteady effects such as shock motion, wake-stator interaction and potential flow separation.

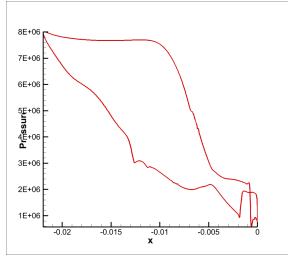


Figure 5.31: Stator blade pressure distribution at time instant t_0

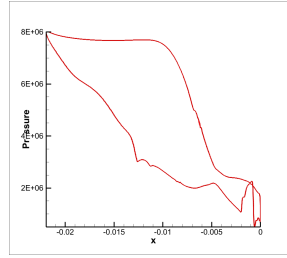


Figure 5.32: Stator blade pressure distribution at time instant t_1

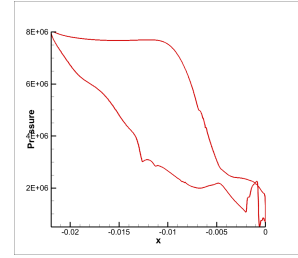


Figure 5.33: Stator blade pressure distribution at time instant t_2

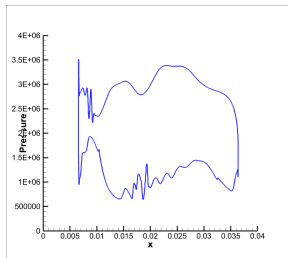


Figure 5.34: Rotor blade pressure distribution at time instant t_0

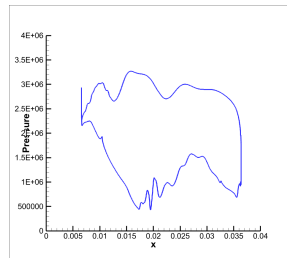


Figure 5.35: Rotor blade pressure distribution at time instant t_1

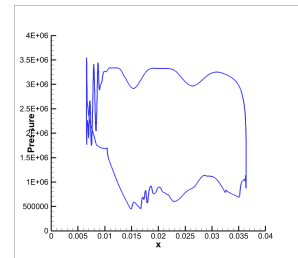


Figure 5.36: Rotor blade pressure distribution at time instant t_2

The stator pressure distribution exhibits slight variations over time, as shown in figures 5.31, 5.32 and 5.33. These fluctuations are indicative of an unsteady interaction with the rotor, especially due to the periodic passage of rotor blades and the associated shock structures.

As expected, the stator displays a more stable pressure profile compared to the rotor. Nevertheless, in the downstream region of the stator blades (near the trailing edge), unsteady effects become more evident, with small oscillations and shifts in the pressure distribution.

In contrast, the rotor blade pressure profiles (Figures 5.34, 5.35, and 5.36) show significant time-dependent fluctuations, highlighting the presence of strong unsteady aerodynamic loads induced by shock motion and rotor–stator interactions.

Following the unsteady analyses, the degree of reaction is recalculated using the time-resolved enthalpy data at different blade sections. The resulting average value of the degree of reaction is approximately $R \approx 0.0014$, which significantly differs from the initially assumed value of 0.25. This low value of R indicates an impulse-type behaviour of the stage, with the rotor carrying out almost the entire enthalpy drop, while the stator primarily serves to direct the flow.

5.4.3 Results Comparison

To evaluate the flow non-uniformities downstream of the stator and how they are influenced by the Mach number at the rotor inlet, the tangential pressure distributions are displayed.

For a proper comparison, the issue of the large post-expansion at the outlet of the second-stage stator is first addressed: the analyses are repeated, considering an outlet pressure equal to the average of the pressure distribution from the unsteady simulations. The resulting Mach number distribution is shown in figure 5.37.

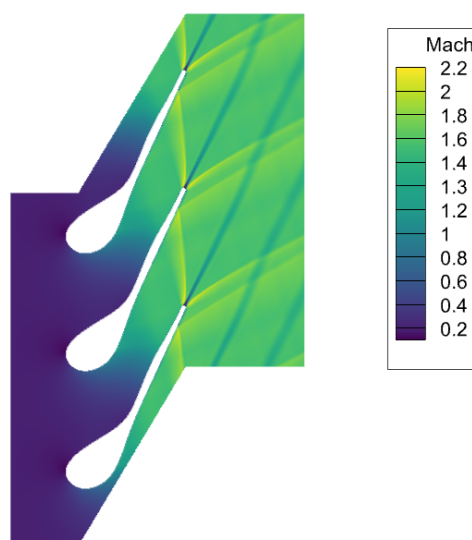


Figure 5.37: Mach number distribution of the second stator with higher downstream pressure

In figure 5.38, the tangential pressure distributions are compared.

It can be observed that the mixing plane method closely follows the average of the harmonic balance solution in the fish-tail region of the stator, the central area of the figure, but exhibits significant differences in the rest of the domain. The pressure distribution obtained with the mixing plane method shows fewer peaks compared to the harmonic balance method, suggesting that the steady approach does not fully capture unsteady effects, such as the upstream propagation of shock waves towards the stator.

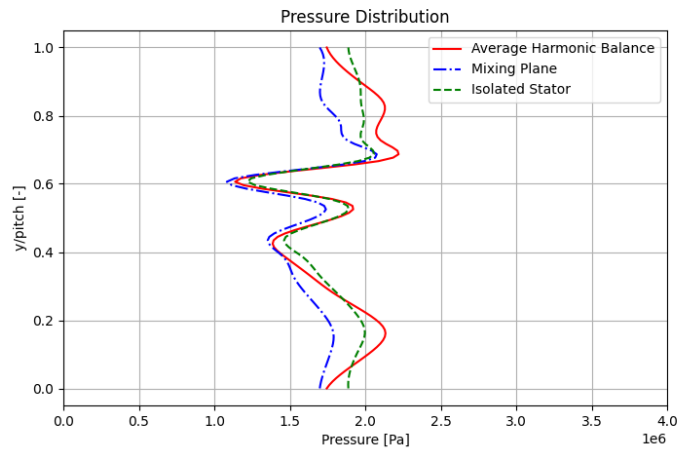


Figure 5.38: Tangential pressure distributions

The isolated stator curve deviates significantly from the other two, highlighting that the absence of the rotor substantially alters the pressure distribution and that an isolated stator analysis may not be sufficient to accurately predict the actual behaviour of the turbine at high Mach numbers. The average pressure value from the isolated stator analysis is closer to that of the HB compared to the MP; however, it should be noted that the downstream pressure value for the isolated stator was corrected and set equal to the average obtained from the HB analysis, whereas the value predicted by TurboSim was significantly lower.

In figure 5.39, the pressure distributions for the three time instances of the harmonic balance method are compared.

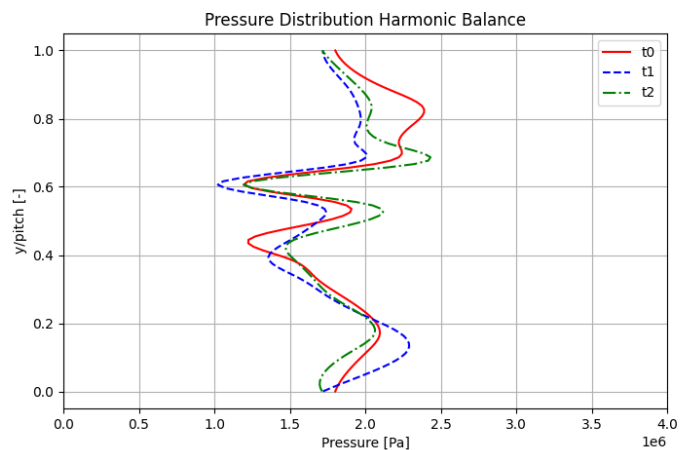


Figure 5.39: Tangential pressure distributions of the unsteady simulations

The pressure varies significantly over time, with pronounced oscillations along the pitch-wise direction. These fluctuations are due to the interaction between the stator and the rotor, particularly the upstream propagation of the bow shock, which is not captured by steady analysis. The oscillatory behaviour confirms the unsteady nature of the problem at these high Mach numbers and suggests that an unsteady approach is necessary for an accurate prediction of the pressure field in the turbine.

Chapter 6

Conclusions

6.1 Summary

This study investigates stator-rotor interactions in supersonic turbines through advanced CFD simulations. The primary objective is to evaluate how representative an isolated stator analysis is of the pitch-wise distribution at the stator outlet, compared to coupled stator-rotor analyses. A key focus is to assess the unsteadiness of the flow and to determine whether steady approaches can still provide reliable results while reducing computational cost.

The central research question concerns how the relative Mach number at rotor inlet influences these interactions. To address this, three turbine stages are designed, each targeting a different rotor inlet Mach number.

The design process is carried out using custom in-house codes, adapted specifically for the problem at hand. Once the 2D profiles are generated, a series of CFD simulations are performed: steady-state analyses of the isolated stator, steady coupled stator-rotor simulations using the mixing plane model and fully unsteady simulations using the harmonic balance method.

From the comparison of the different methods, it can be concluded that under high Mach number conditions, steady-state approaches, both isolated stator and coupled stator-rotor, do not provide sufficient accuracy to assess turbine performance. This is particularly evident when considering the potential inaccuracies of mean-line methods in predicting downstream or post-expansion pressure values.

Given these limitations, stator-rotor analysis are always preferable when computational resources are available. Even better, unsteady simulations should be adopted, as they provide a more accurate representation of the flow phenomena.

6.2 Future Developments

To fully understand when unsteady simulations become essential, future investigations should include harmonic balance analyses of both low and high expansion ratio stages, since this work focused only on the medium expansion case. This would help determine under which conditions unsteady analysis becomes necessary and when steady-state stator-rotor simulations remain adequate. At higher Mach numbers, the bow shock tends to thicken and intensify, potentially causing stronger unsteady interactions.

A meaningful extension of this study would include a comparison of the stator outlet tangential pressure distributions for the other two turbine stages. Additionally, evaluating the tangential distribution of efficiency could provide further insight into the robustness of the design under varying flow conditions.

It should also be noted that the rotor blade profiles used in this study feature sharp leading and trailing edges. While this geometry is useful for conservative aerodynamic predictions, since it tends to amplify shock strength and boundary layer interaction, it is not realistic for manufacturing purposes. In practice, the leading edge must be rounded to ensure structural integrity and thermal resistance, especially in high-temperature environments. This necessary adjustment should be addressed in the detailed design phase and may slightly modify the shock structure and flow behaviour observed in the numerical analysis.

This work also has practical applications. The tools and methods used form a base for future turbine design. They can help improve performance and make the design process more efficient, even in complex flow conditions.

Appendix A

Design Maps

First Turbine Stage

The output maps for the first turbine stage ($\beta = 5$) are as follows. They are computed at fixed degree of reaction ($R = 0.25$) and *flaring* = 10° .

Firstly, a rotor inlet Mach number of 0.9 should be the target, so to follow the guidelines it is fundamental to consider the maps that are plotted in figures A.1, A.2, A.3, A.4. The loading coefficient should be high as well as the peripheral speed.

At the same time, TurboSim fails to calculate some designs, particularly for high K_{is} and low ϕ . This can be explained by the losses becoming too high, in particular the boundary layer losses do not converge in that area, as in the figure A.5.

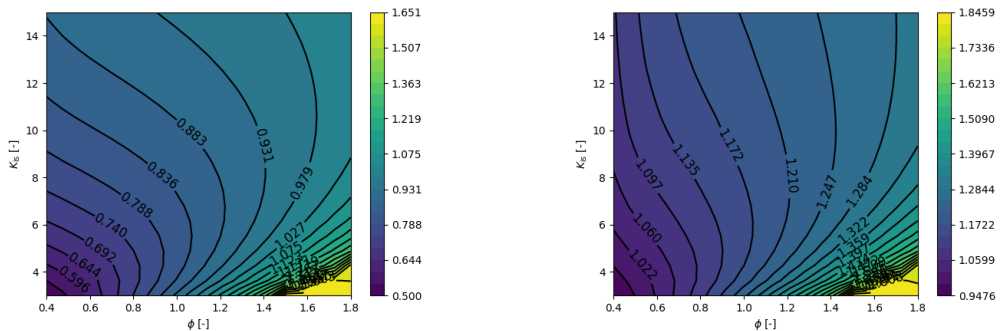


Figure A.1: Rotor inlet Mach number **Figure A.2:** Rotor outlet Mach number

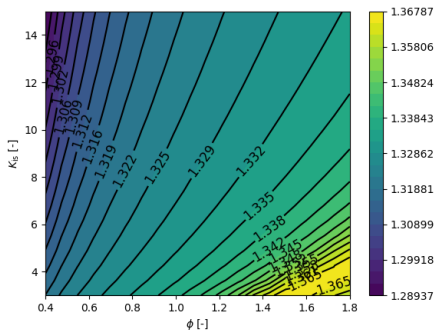


Figure A.3: Stator outlet Mach number

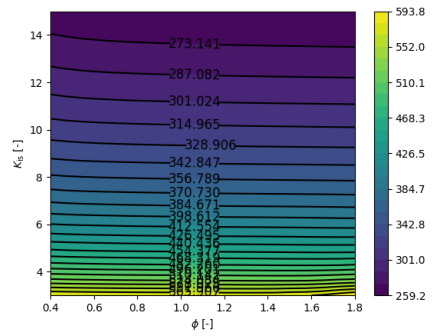


Figure A.4: Peripheral speed

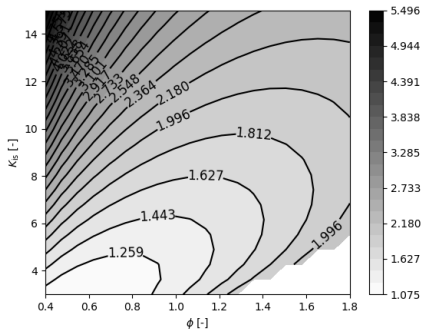


Figure A.5: Boundary Layer Losses

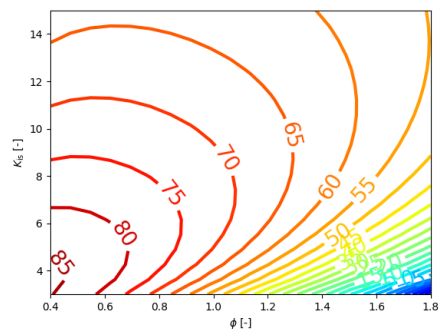


Figure A.6: Total-to-static Efficiency

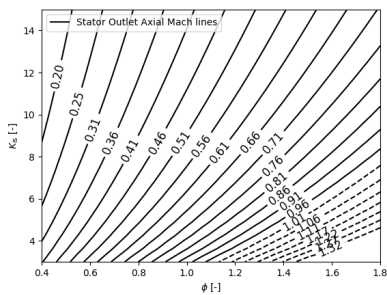


Figure A.7: Stator outlet and rotor inlet axial Mach number

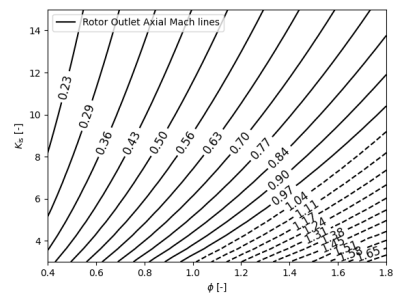


Figure A.8: Rotor outlet axial Mach number

Total-to-static efficiency (figure A.6) is considered rather than the total-to-total one, as explained in the previous paragraph. Furthermore, the axial Mach numbers are plotted as they must be subsonic in figures A.7 and A.8.

Therefore, from this point forward, the regions described by the dotted lines are not considered for a possible solution, in particular the area where the axial Mach number exiting the rotor is greater than 1, as this is a more conservative approach.

Before choosing a design for the analysis, it is important to examine other parameters, particularly those concerning the guidelines explained above, such as in the figures A.9, A.10, A.11. So, the maps of rotor outlet absolute Mach number, rotor outlet flow angle and stator outlet flow angle are plotted considering the delayed zone and the rotor inlet Mach number, as this parameter is the target of this analysis.

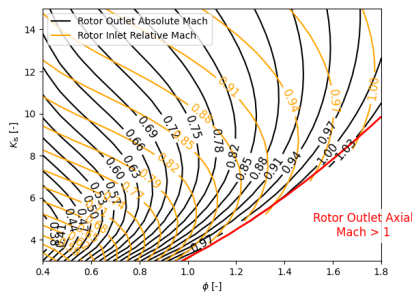


Figure A.9: Rotor outlet absolute Mach number

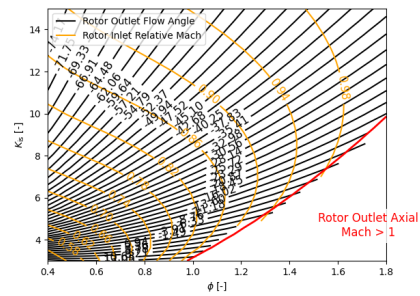


Figure A.10: Rotor outlet flow angle [°]

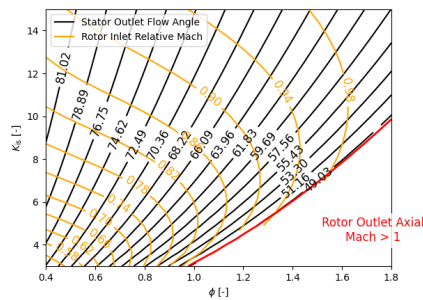


Figure A.11: Stator outlet flow angle [°]

Moreover, after dimensioning, other maps are computed, as shown in figures

A.12, A.13 and A.14, to get a clearer idea of the heights and diameter of the turbine stage.

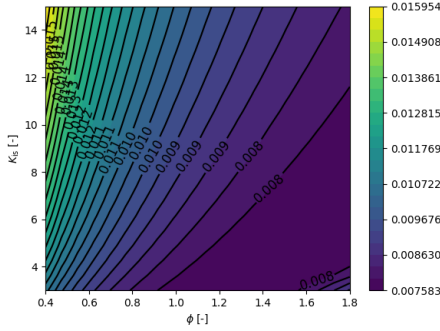


Figure A.12: Stator Inlet Blade Height (H_0) [m]

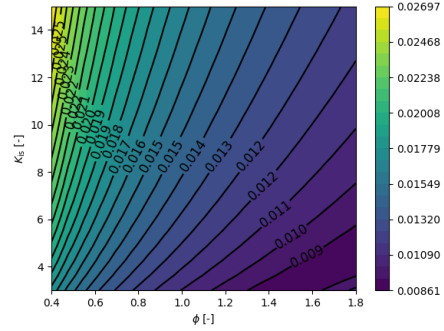


Figure A.13: Stator Outlet Blade Height ($H_1 = H_2$) [m]

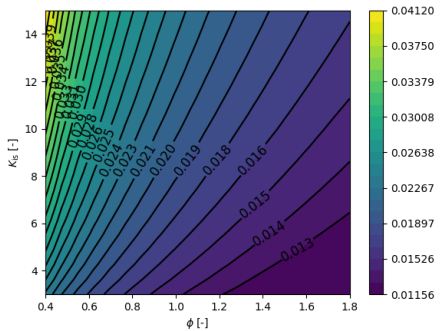


Figure A.14: Rotor Outlet Blade Height (H_3) [m]

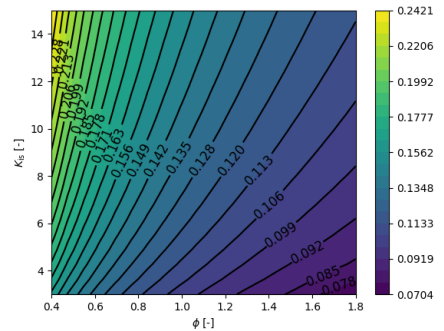


Figure A.15: Mean Diameter [m]

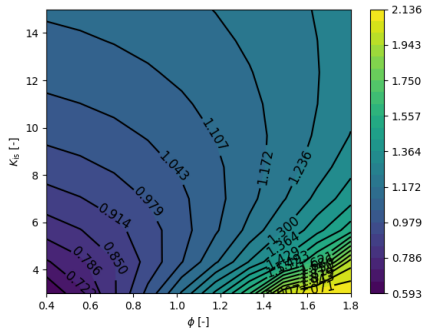
Second Turbine Stage

The resulting maps are also analysed for the second stage of the turbine. They exhibit similar characteristics to those of the first stage.

In particular, the Mach number and peripheral speed are higher, as expected, due to the higher expansion ratio (figures A.16, A.17, A.18, A.19).

Furthermore, the efficiency maps is shown in figure A.20.

The maps of rotor outlet absolute Mach number, rotor outlet flow angle and stator outlet flow angle are plotted considering the delayed zone and the rotor inlet Mach number (figures A.21, A.22, A.23).



In this case as well, the difficulties are likely related to the losses generated by the specific combination of duty coefficients within this region.

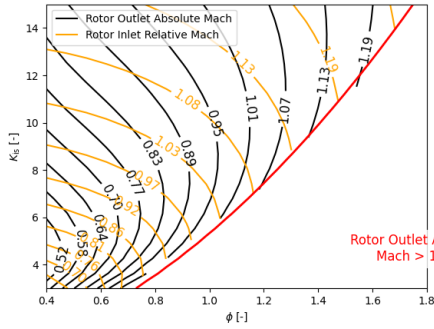


Figure A.21: Rotor outlet absolute Mach number

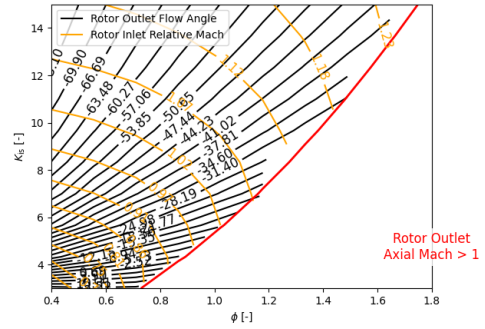


Figure A.22: Rotor outlet flow angle $[\circ]$

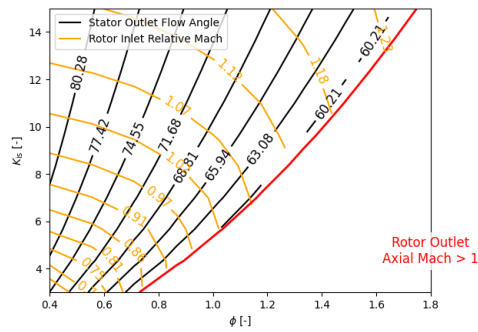


Figure A.23: Stator outlet flow angle $[\circ]$

Third Turbine Stage

In the case of the third stage, the pressure ratio is really high and this is clear from all the maps, where there is always the same area that does not work but is more extensive.

In particular, the Mach number and peripheral speed are higher, as expected due to the higher expansion ratio (figures A.24, A.25, A.26, A.27).

Furthermore, the efficiency map is shown in figure A.28.

The maps of rotor outlet absolute Mach number, rotor outlet flow angle and stator outlet flow angle are plotted considering the delayed zone and the rotor inlet Mach number (figures A.29, A.30 and A.31).

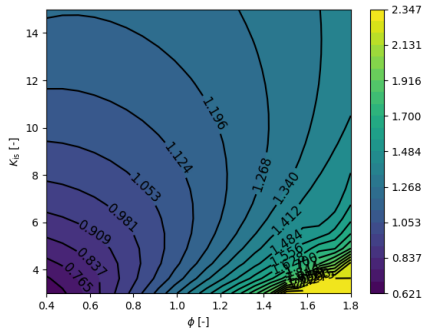


Figure A.24: Rotor inlet Mach number

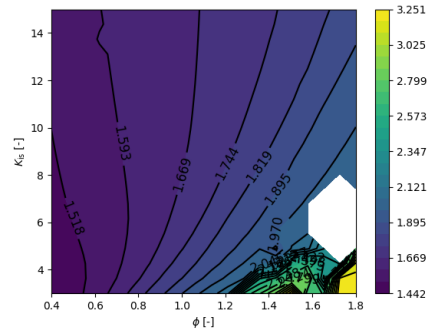
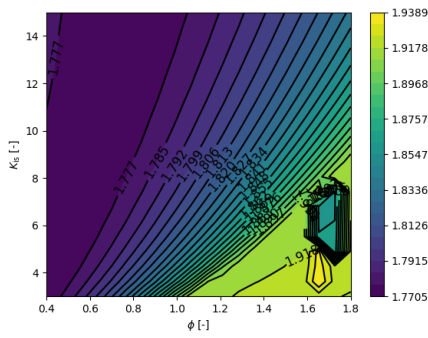


Figure A.25: Rotor outlet Mach number



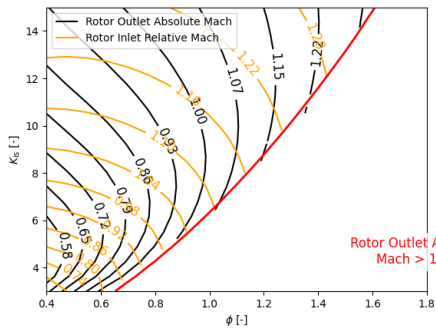


Figure A.29: Rotor outlet absolute Mach number

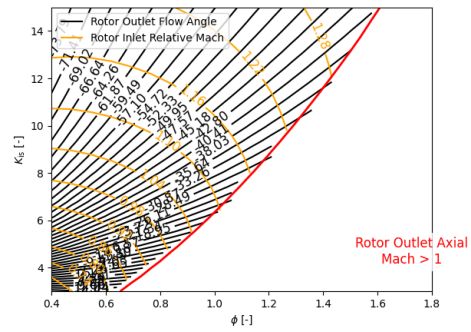


Figure A.30: Rotor outlet flow angle [°]

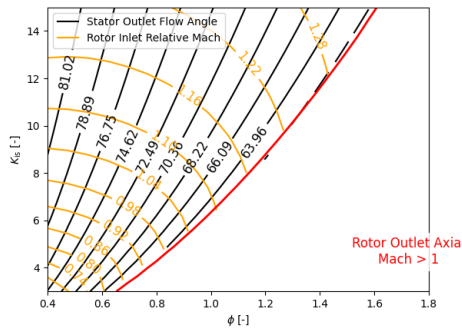


Figure A.31: Stator outlet flow angle [°]

It is still possible to notice, and in a more noticeable manner in the third case, how the zone in which the designs do not converge in the maps also corresponds with the zone in which the axial Mach becomes greater than 1 and is therefore to be avoided in any case.

This turbine stage is crucial for choosing a final design for the subsequent analysis, because it is the most limited case with respect to the guidelines.

Bibliography

- [1] G. Paniagua, M. C. Iorio, N. Vinha, and J. Sousa. «Design and analysis of pioneering high supersonic axial turbines». In: *International Journal of Mechanical Sciences* 89 (Aug. 2014), pp. 65–77. DOI: 10.1016/j.ijmecsci.2014.08.014 (cit. on p. 2).
- [2] Arthur J. Glassman. *Turbine Design and Application*. NASA SP-290. Available from NASA Center for Aerospace Information, Linthicum Heights, MD. Washington, DC: National Aeronautics and Space Administration (NASA), 1994 (cit. on pp. 3, 32).
- [3] Chao Fu, Zhengping Zou, Qingguo Kong, Honggui Cheng, and Weihao Zhang. «Aerodynamic Design and Numerical Analysis of Supersonic Turbine for Turbo Pump». In: *International Journal of Turbo & Jet-Engines* 33.3 (Aug. 2016), pp. 239–252. DOI: 10.1515/tjj-2015-0028 (cit. on p. 3).
- [4] Bhupinder Singh Sanghera, Nitish Anand, Louis Souverein, Loïc Penin, and Matteo Pini. «Adjoint-Based Optimisation of Rocket Engine Turbine Blades». In: *Proceedings of ASME Turbo Expo 2021: Turbomachinery Technical Conference and Exposition*. GT2021-59580. ASME. Virtual, Online, June 2021 (cit. on pp. 3–5).
- [5] Kaname Kawatsu, Naoki Tani, Mitsuru Shimagaki, Masaharu Uchiumi, Nobuhiro Yamanishi, Katsunori Mitsuhashi, and Tsutomu Mizuno. «Multi-Objective Optimization of a Supersonic Axial Turbine Blade Row Shape for a Rocket Engine Turbopump». In: *47th AIAA/ASME/SAE/ASEE Joint Propulsion Conference & Exhibit*. AIAA 2011-5784. American Institute of Aeronautics and Astronautics (AIAA). San Diego, California, July 2011. DOI: 10.2514/6.2011-5784 (cit. on p. 3).
- [6] George P. Sutton and Oscar Biblarz. *Rocket Propulsion Elements*. 9th. Hoboken, NJ: John Wiley & Sons, 2016. ISBN: 978-1-118-75365-1 (cit. on p. 4).
- [7] S. L. Dixon and C. A. Hall. *Fluid Mechanics and Thermodynamics of Turbomachinery*. 6th. Oxford, UK: Butterworth-Heinemann, 2010 (cit. on pp. 8, 10, 21, 22).

-
- [8] Andrea Giuffre and Matteo Pini. «Design Guidelines for Axial Turbines Operating With Non-Ideal Compressible Flows». In: *Journal of Engineering for Gas Turbines and Power* 143.1 (2021), p. 011004. DOI: 10.1115/1.4049137 (cit. on pp. 13–16, 18).
- [9] D.J. Mee, N.C. Baines, M.L.G. Oldfield, and T.E. Dickens. «An Examination of the Contributions to Loss on a Transonic Turbine Blade in Cascade». In: *ASME 1990 International Gas Turbine and Aeroengine Congress and Exposition*. American Society of Mechanical Engineers. 1990, V005T16A012. DOI: 10.1115/90-GT-264 (cit. on p. 17).
- [10] D. G. Wilson. «New Guidelines for the Preliminary Design and Performance Prediction of Axial-Flow Turbines». In: *Proceedings of the Institution of Mechanical Engineers* 201.A4 (1987), pp. 219–290 (cit. on pp. 19, 20, 22).
- [11] Guillermo Paniagua, Michele C. Iorio, Nuno Vinha, and Jorge Sousa. «Design and analysis of pioneering high supersonic axial turbines». In: *International Journal of Mechanical Sciences* 89 (2014), pp. 65–77. DOI: 10.1016/j.ijmecsci.2014.09.002 (cit. on p. 20).
- [12] Ronald H. Aungier. *Turbine Aerodynamics: Axial-Flow and Radial-Flow Turbine Design and Analysis*. ASME Press, 2006. ISBN: 9780791802467 (cit. on pp. 21, 22, 66).
- [13] J. Blazek. *Computational Fluid Dynamics: Principles and Applications*. Amsterdam, London, New York, Oxford, Paris, Shannon, Tokyo: Elsevier, 2001. ISBN: 0080430090 (cit. on pp. 29, 45, 46, 48–54, 56, 65).
- [14] Nitish Anand, Salvatore Vitale, Matteo Pini, Gustavo J. Otero, and Rene Pecnik. «Design Methodology for Supersonic Radial Vanes Operating in Nonideal Flow Conditions». In: *Journal of Engineering for Gas Turbines and Power* 141.2 (2019), pp. 022601-1–022601-9. DOI: 10.1115/1.4040182 (cit. on pp. 30, 33–35, 37).
- [15] M. Zucrow and J. Hoffman. *Gas Dynamics*. Vol. I and II. Wiley & Sons, 1976, p. 297 (cit. on p. 30).
- [16] Roland Span, Wolfgang Wagner, Eric W. Lemmon, and Richard T. Jacobsen. «Multiparameter equations of state — recent trends and future challenges». In: *Fluid Phase Equilibria* 183–184 (2001), pp. 1–20. DOI: 10.1016/S0378-3812(01)00416-2 (cit. on p. 35).
- [17] Nitish Anand, Piero Colonna, and Matteo Pini. «Design Guidelines for Supersonic Stators Operating with Fluids Made of Complex Molecules». In: *Energy* 203 (2020), p. 117698. DOI: 10.1016/j.energy.2020.117698 (cit. on pp. 35, 36).

- [18] Alessandro Cappiello and Raffaele Tuccillo. «Design Parameter Influence on Losses and Downstream Flow Field Uniformity in Supersonic ORC Radial-Inflow Turbine Stators». In: *International Journal of Turbomachinery, Propulsion and Power* 6.3 (2021), p. 38. DOI: 10.3390/ijtp6030038 (cit. on pp. 37, 42).
- [19] Pulkit Aggarwal. «Supersonic Axial & Radial Rotor Design for ORC Applications Using Method of Characteristics». MA thesis. Delft University of Technology, 2018 (cit. on pp. 38, 39).
- [20] Kaname Kawatsu, Naoki Tani, and Nobuhiro Yamanishi. «Numerical Study on Rotor-Stator Interaction of a Supersonic Reaction Turbine for a Liquid Rocket Engine». In: *Proceedings of ASME 2010 3rd Joint US-European Fluids Engineering Summer Meeting and 8th International Conference on Nanochannels, Microchannels, and Minichannels (FEDSM2010-ICNMM2010)*. ASME, Montreal, Canada, Aug. 2010, FEDSM2010-ICNMM2010-30640 (cit. on p. 43).
- [21] Michael B. Giles. «Stator/Rotor Interaction in a Transonic Turbine». In: *Journal of Propulsion and Power* 6.5 (Sept. 1990), pp. 621–627. DOI: 10.2514/3.23263 (cit. on pp. 43, 44, 64).
- [22] R. J. Miller, R. W. Moss, R. W. Ainsworth, and N. W. Harvey. «Wake, Shock, and Potential Field Interactions in a 1.5 Stage Turbine—Part I: Vane-Rotor and Rotor-Vane Interaction». In: *Journal of Turbomachinery* 125.1 (2003), pp. 33–41. DOI: 10.1115/1.1508386 (cit. on p. 43).
- [23] Guillermo Paniagua, Tolga Yasa, Andres de la Loma, Lionel Castillon, and Thomas Coton. «Unsteady Strong Shock Interactions in a Transonic Turbine: Experimental and Numerical Analysis». In: *Journal of Propulsion and Power* 24.4 (2008), pp. 722–731. DOI: 10.2514/1.34774 (cit. on p. 43).
- [24] Filippo Rubecchini, Michele Marconcini, Matteo Giovannini, Juri Bellucci, and Andrea Arnone. «Accounting for Unsteady Interaction in Transonic Stages». In: *Journal of Engineering for Gas Turbines and Power* 137.5 (2015), p. 052602. DOI: 10.1115/1.4028667 (cit. on pp. 44, 57).
- [25] P.G. Tucker. *Unsteady Computational Fluid Dynamics in Aeronautics*. Vol. 104| Fluid Mechanics and Its Applications. Dordrecht, Heidelberg, New York, London: Springer, 2014. DOI: 10.1007/978-94-007-7049-2 (cit. on pp. 45, 53, 56).
- [26] R. Courant, K. Friedrichs, and H. Lewy. «Über die partiellen Differenzengleichungen der mathematischen Physik». In: *Mathematische Annalen* 100.1 (1928), pp. 32–74 (cit. on pp. 51, 52).
- [27] David C. Wilcox. *Turbulence Modeling for CFD*. Third. La Cañada, California: DCW Industries, Inc., 2006. ISBN: 978-1-928729-08-2 (cit. on pp. 54, 55).

- [28] S. Vitale, M. Pini, and P. Colonna. «Multistage Turbomachinery Design Using the Discrete Adjoint Method Within the Open-Source Software SU2». In: *Journal of Propulsion and Power* 36.3 (2020), pp. 465–478. DOI: 10.2514/1.B37685 (cit. on p. 56).
- [29] J. D. Denton. «Some Limitations of Turbomachinery CFD». In: *Proceedings of the ASME Turbo Expo 2010: Power for Land, Sea, and Air*. GT2010-22540. Glasgow, UK: ASME, June 2010 (cit. on p. 57).
- [30] A. Rubino, M. Pini, P. Colonna, T. Albring, S. Nimmagadda, T. Economon, and J. Alonso. «Adjoint-based fluid dynamic design optimization in quasi-periodic unsteady flow problems using a harmonic balance method». In: *Journal of Computational Physics* 372 (2018), pp. 220–235. DOI: 10.1016/j.jcp.2018.06.023 (cit. on p. 57).
- [31] L. He. «Fourier methods for turbomachinery applications». In: *Progress in Aerospace Sciences* 46.5-6 (2010), pp. 329–341. DOI: 10.1016/j.paerosci.2010.04.001 (cit. on pp. 58, 59).
- [32] ANSYS, Inc. *Ansys TurboGrid User’s Guide*. Release 2021 R2. Accessed: 2025-02-13. ANSYS, Inc. Canonsburg, PA, USA, July 2021 (cit. on p. 61).
- [33] P. J. Roache. «Perspective: A Method for Uniform Reporting of Grid Refinement Studies». In: *Journal of Fluids Engineering* 116.3 (1994), pp. 405–413. DOI: 10.1115/1.291 (cit. on p. 62).
- [34] Antonio Rubino, Piero Colonna, and Matteo Pini. «Adjoint-Based Unsteady Optimization of Turbomachinery Operating with Nonideal Compressible Flows». In: *Journal of Propulsion and Power* 37.6 (2021), pp. 910–918. DOI: 10.2514/1.B37920 (cit. on p. 62).
- [35] Delft High Performance Computing Centre (DHPC). *DelftBlue Supercomputer (Phase 2)*. <https://www.tudelft.nl/dhpc/ark:/44463/DelftBluePhase2>. 2024 (cit. on p. 63).
- [36] Rodrick V. Chima. *Calculation of Multistage Turbomachinery Using Steady Characteristic Boundary Conditions*. Tech. rep. NASA Lewis Research Center, 1998 (cit. on p. 64).
- [37] Hans W. Liepmann and Anatol Roshko. *Elements of Gasdynamics*. John Wiley & Sons, 1957. ISBN: 9780471029973 (cit. on p. 66).

